title

Numerical study of the conversion of methane to hydrogen and carbon in a heated methane-argon flow with seed carbon nano particles

R. Sewgolam

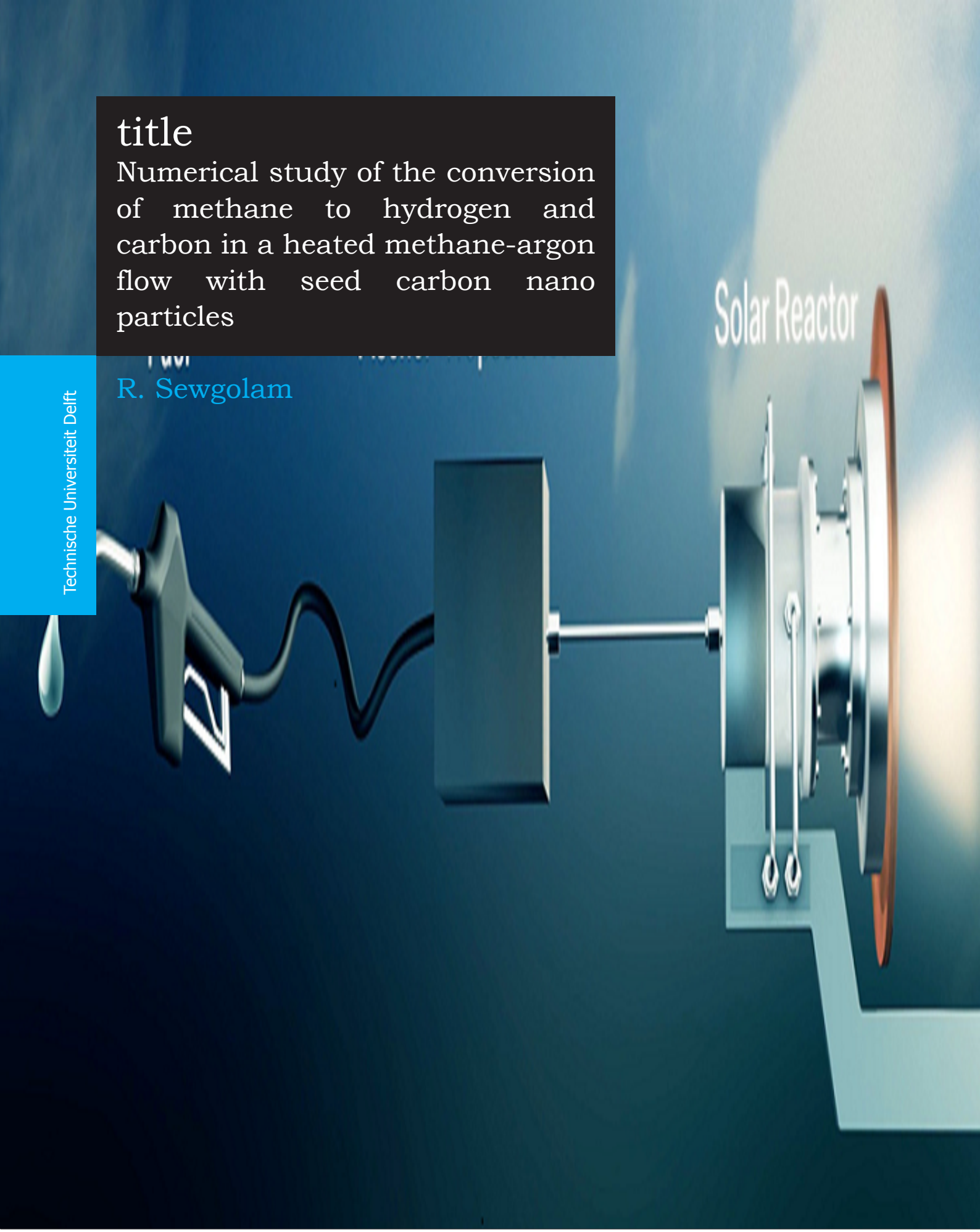

Technische Universiteit Delft

TU Delft Delft University of Technology

Challenge the future

title

Numerical study of the conversion of methane to hydrogen and carbon in a heated methane-argon flow with seed carbon nano particles

by

Sewgolam

in partial fulfillment of the requirements for the degree of

Master of Science
in Mechanical Engineering

at the Delft University of Technology,
to be defended publicly on March 14, 2018 at time 14.00

Supervisor :	Prof. Dr. Dirk Roekearts	
co-supervisor :	Ir. Simone. Silvestri	
Thesis committee:	Prof. Dr. D.J.E.M Roekearts	TU Delft
	Dr. ir. M. J Tummers	TU Delft
	Dr. ir. J. W Haverkort	TU Delft
	Ir. S. Silvestri	TU Delft

TU Delft Delft University of Technology

Abstract

In this work numerical simulations are performed on the decomposition of methane gas into hydrogen gas and solid carbon particles in a solar reactor. The process can contribute to development of technology of energy production from natural gas with zero CO2 emission technology. First an overview of solar reactor designs for cracking of methane developed throughout the years is presented and summarized in a table. Next the computational study focuses on modeling of methane decomposition in a tubular reactor taking into account radiative heat transfer and heterogeneous reaction on the surface of the particles. The numerical simulation is performed using of ANSYS fluent 17.2 sofware to solve the following: Navier-Stokes equation for fluid dynamics, the radiative heat transfer equation for radiation absorption by methane and particle species, the advection-diffusion-reaction equation for the gas and particle species transport. The governing equations are presented in dimensionless form to see which physical phenomena are dominant in the system. When methane decomposes, the produced solid carbon sticks on the surface of the seed carbon particles, which grow in diameter. During the simulations the influence of the following parameters was examined, initial particle volume fraction (either 10^{-5} or 10^{-4}), wall heat flux (10 kW or 15 kW), reactor length (600mm or 1000mm) and initial methane mole fraction (in a mixture with argon). In all cases a laminar temperature boundary layer develops inside the reactor. When temperature is high enough in this boundary layer methane is cracked into hydrogen. From the results the following can be concluded. Increasing the particle volume fraction from 10^{-5} to 10^{-4} enhances the methane conversion from 12 % to 23 %. Second increasing the wall heat flux from 10 kW to 15kW enhances the methane conversion further from 23 % to 61 % . Alternatively extending the reactor length from 600 mm to 1000mm enhances the methane conversion from 23 % to 72 %. Finally decreasing the methane mole inlet fraction from 0.297 to 0.1 increases the methane molar conversion from 22 % to 42 %. Recommendations for further work are made.

Contents

List of Figures

List of Tables

1

Introduction

1.1. General information

The widespread use of fossil fuels (coal, petroleum,natural gas) has increased enormously due to rising energy demand,mainly for transport and generation of electricity, steam etc. Energy demand is growing fast(5 % per year 2010-2015),and increasingly requires more fossil fuels resources to be exploited, in order to meet the energy requirements worldwide. Growth in demand happens not only in industrial well developed countries, but also in large transitional economies (China, India), and developing countries. Fossil fuels contain high percentages of carbon. Depending on the fossil fuel it can contain a range of volatile materials with low carbon to hydrogen ratios. Those organic compound consisting entirely of carbon and hydrogen are known as hydrocarbons. When the hydrocarbons(fossil fuels) are burned to release energy the reactants product(emissions) do pollute the environment. Such contamination is causing serious damage to life on earth through the speeding up of climate change and by causing a range of serious health problems. One of the most important emissions attributable to hydrocarbon combustion is carbon dioxide(CO_2). To reduce carbon dioxide emissions scientists throughout the world are working on renewable energy resources. Private and governments institutions are investing in biomass, solar and wind power plants to reduce fossil fuel consumption in the near future and thereby, also carbon dioxide emissions. However, before the energy demand can be met by renewable energy resources, an elaborate process transition must take place. To deal with the carbon dioxide emission problem in the short to mid-term future, natural gas, which is present in large quantities can be used. Natural gas has lower emissions of carbon dioxide comparing with other fossil fuels like coal and oil, and might be a suitable candidate for the transition towards a sustainable development of renewable energies. When natural gas is burned and converted less carbon dioxide is produced per unit mass than burning of oil or coal. Alternatively to completely avoid the carbon dioxide emission when natural gas is used to produce energy, Natural gas can be decomposed into solid carbon particles and hydrogen gases in a solar reactor. In the solar reactor concentrated solar radiation is used to heat natural gas in such a way that no carbon dioxide is produced. Although natural gas is a fossil fuel type, when using natural gas in combination with concentrated solar radiations as heat source no carbon dioxide is produced, which is a step towards sustainable resources. The incoming solar radiation is almost free energy which is used as heat source, This process is known as cracking of natural gas (methane) into carbon solid particle and hydrogen gases. Depending on the quality of carbon particles they can be used in industrial application. The main usefull product is the energy carrier which is hydrogen gas. The hydrogen gas can be directly used as energy source for different applications. Another up coming technology which is currently in the research phase is the development of the fuel cells where the carbon particles and hydrogen gas can be used to generate electric power. The fuel cell is an electrochemical cell that converts the chemical energy from a fuel into electricity through an electrochemical reaction of hydrogen fuel with oxygen or another oxidizer agent.

1.2. Cracking of natural gas in solar reactor

In the solar reactor, hydrogen gas and carbon particles are produced by thermal cracking of the natural gas, where the required heat is supplied by solar radiation. The advantage of using heat coming from

the sun for hydrogen production is as follows :

- Zero carbon dioxide emissions
- The solar energy supply is available for free

As known, hydrogen gas is an energy carrier which can be used in fuel cells to produce electricity or can be burned directly. The solar cracking process of natural gas, oil and other hydrocarbon is given by the following reaction overall equations (1.1).

$$C_x H_y = xC(s) + \frac{y}{2} H_2 \tag{1.1}$$

Equation (1.1) indicates a general reaction step when methane is cracked into carbon solid particles and hydrogen-rich gas when the assumption is made that no byproduct is form during the reaction. After some purification step of the reaction product carbon and hydrogen gas can be separated and stored for further use. Although the production of hydrogen gas is the main product, carbon solid particle can be used as commodity material in rubber industrial application depending on the quality of this product. Another possibility of using the carbon particles is in direct carbon fuel cells [8]. This additional use of carbon was also mentioned by Prof.N.Ozalp during a guest lecture at the Delft University of Technology on 6 June 2017. In the carbon fuel cell, carbon dioxide and electricity are produced. Before the carbon fuel cell can be used in combination with the solar reactor, there is still much research to be done. However in the master thesis of A. Rubino at Delft University of Technology [9], four possible viable options are analyzed as follows :

- Carbon (solid) is sequestered and only hydrogen is used in a fuel cell.
- Carbon (solid) is used to fuel a conventional Rankine cycle and hydrogen is used in a fuel cell.
- Syngas is produced by solar steam gasification of C and further processed to H_2 and used in a fuel cell together with the H_2 produced by the solar thermal cracking
- Carbon is used as a reduction agent for a 2 step thermochemical cyclic process for the production of hydrogen using water splitting and a metal oxide as energy carrier or storage.

The currently existing solar reactor design are based on two concepts:

- **first** Direct solar radiation: In this case the natural gas (methane gas) is directly exposed to concentrated solar radiation. Natural gas has a low absorption coefficient in the visible range of light, which makes it very hard to heat the natural gas directly by the concentrated radiation. To solve this problem, additional nanometer size carbon particles are injected. The additional carbon particles have a higher absorption coefficient and are capable to absorb the solar radiation of the sun. Once the particles are heated up, the heat transfer from the particle to methane by convection is efficient. When the reaction starts, carbon particles grow and extra particles can be produced.

- **second** Indirect solar radiation: In this case the wall of the pipe containing natural gas is heated by the solar radiation and subsequently the energy is transferred to the gas by convection, conduction and radiation. Because of additional heat transfer resistance significant differences in operation compared to the first method exist.

  Independent of the reactor design once the reactor is at reaction temperature, carbon particles will be produced and these can deposited on walls. The deposition of carbon on the walls will block the heat transfer to the medium and cause clogging problems.

1.3. Thesis objective

As will be seen in a historical overview of solar reactor design (chapter 2), there is an increasing interest in understanding several important aspects. The literature study shows the bottlenecks at the current research stage. The first goal of this thesis is to provide a good overview of the design and identifying the bottlenecks. The second goal is to non dimensionalize the governing equations and

identify which terms are dominant. The last goal is to develop a simple 2D computational fluid dynamic (CFD) simulation in ANSYS Fluent to understand what happens inside a solar reactor. Finally from the simulation results conclusion will be drawn on how reactor design influences methane conversion and hydrogen production.

1.4. Thesis outline

This master thesis consists of 5 chapters. In chapter 1, general information has been given about why solar reactors are important to study and the basic working principles. Chapter 2 presents a historical overview of different solar reactor designs developed throughout the years. Chapter 3 presents the fundamental equations and the radiation theory. In chapter 4 the result will be presented, discussed and validated with literature study. Finally the conclusions and recommendations will be presented in Chapter 5.

2

Solar reactor designs development throughout the years

Throughout the years several solar reactor designs have been developed and studied extensively. Before performing calculation it is extremely important to understand what kind of problem must be dealed with when designing or improving a existing solar reactor. In the literature several solar reactor designs were found which had been studied. Depending on the solar reactor design concept explained in chapter one and the design itself, the solar reactor design which is found in literature can be divided into five groups as follows:

- Cavity receiver indirect solar reactor
- Drop tube indirect solar reactor
- Cavity receiver vortex flow direct solar reactor
- Cavity receiver direct solar reactor
- Aero shield cyclone direct solar reactor

For some solar reactor designs more detailed studied have been perform forn others. Depending on the focus point of the research on the design several adjustment was made to improved the reactor. Due to this the methane conversion was increased and the radiation heat losses was reduced. It is mentioned almost in every solar reactor design that clogging is a major problem. Beside the clogging issue different parameters was studied during numerical or experimental studies. In the rest of this chapter a summary will be given for the five reactor groups.

2.1. Cavity receiver indirect solar reactor

A 10 KW cavity receiver solar reactor based on indirect solar radiation was designed by Rodat *et al.* [1]. In Figure 2.1 the cavity receiver solar reactor is shown.

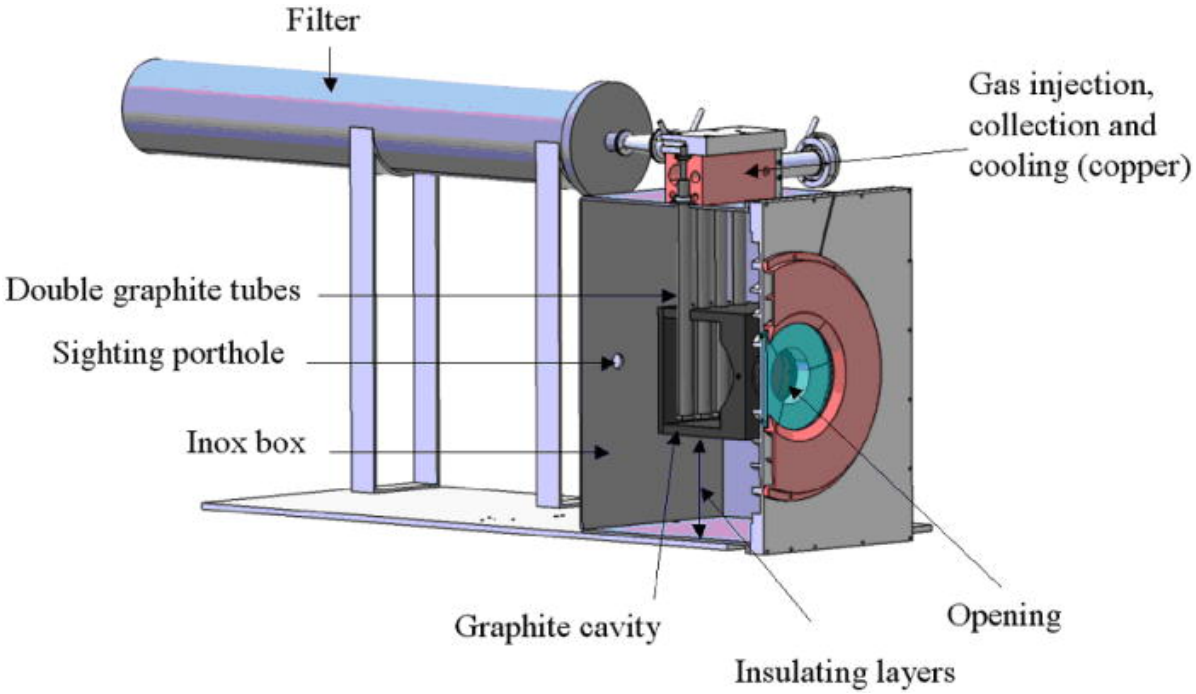

Figure 2.1: Cavity receiver indirect solar reactor design [Rodat *et al.* [1]].

As shown in figure 2.1 the solar reactor contains four tubes. Concentrated solar radiation enters from the opening(window) and heats the tubes inside the graphite cavity. At the top of the reactor methane is injected which is heated inside the tubes. The filter is used to separate the reactant product. It is mentioned that during the experiments a methane conversion and hydrogen yields of 98% and 90% were achieved. During the experiment the tube temperature was $1770K$, the residence time 32 ms and the methane inlet molar fraction was set to 10 %. Beside reactant product carbon and hydrogen gas also acetylene was present as a important byproduct. The resident time and the temperature was controlled during the experiment and the influence of it were examined. A simulation of the experiment shows that the temperature was quite homogeneous in the solar reactor and further there was enormous heat loss due to IR-radiation escaping. The result of the simulation showed that in the irradiation part inside the graphite cavity, the wall and the gas were at the same temperature. However outside the cavity the graphite tube wall is isolated as shown in figure 2.1. Due to this the wall of the tube in the isolated region is colder than the gas flowing inside from the hot region to the cold region. The carbon particles in the gas mixture are then depositing on the cold wall of the tubes inside the isolating region. A following study on kinetic modeling simulation was performed by Rodat *et al.* [10] for the same solar reactor type. The results showed a good correspondence with the experimental results and also other byproducts were identified.

To build the solar reactor for industrial scale a pilot scale solar reactor study was performed by Rodat *et al.* [11]. In his work the influence of temperature in the range of $1608 - 1928$ K and the residence times $37 - 71$ ms on methane conversion and hydrogen yields were examined. Carbon and hydrogen yields of 88% and 49% were obtained at a reactor temperature of 1800 K. In this pilot project it was found that the front face must be drastically improved to reduce the thermal losses. With an optimized design 77% rather than 68% thermal efficiency could be achieved of the maximum thermal energy. A methane conversion between 72% and 100% was obtained. The carbon yield had a maximum value of 63% due to the significant production of acetylene as byproduct. In Maag *et al.* [12] a reactor model was formulated by coupling radiation, convection, conduction heat transfer and chemical kinetics for two phase solid gas reacting flow. The model was validated by experimental results taken by the pilot scale up and used to optimize and estimate the performance of a 10 MW scaled up reactor for a solar tower system. For a methane mass flow rate of 0.7 kilogram per second complete conversion was achieved at 1870 K, which yielded a solar to chemical energy conversion of 42 %. In case of a temperature of 1600 k and when the mass flow was doubled the efficiency was increasing from 42 % to 60 %. The main

consequence of reducing the temperature was that the carbon black quality reduced. Caliot *et al.* [7] developed a two dimensional model of methane thermal decomposition reactor. The model accounted for coupled radiative heat transfer and polydispersed carbon particle nucleation, growth and transport. The model was applied to a tubular laminar reactor flow. The results showed that three regions can be identified. A preheating zone, a reaction zone and a post reaction zone. In the preheating zone no reaction occured. The reason of no reaction in the preheat zone is because of the low absorption coefficient of methane. In the reaction zone, particles are present, which have higher absorption coefficient. Another important conclusion obtained by this works was that the particle distribution varies significantly across the diameter of the tube. A follow up study was performed by Gautier *et al.* [13]. The influence of temperature and pressure on the particles size distribution during the methane cracking process was studied. The results showed that when temperature and pressure increased, the particle size distribution shift, to lower particle sizes.

2.2. Drop tube indirect solar reactor

A second solar reactor is the drop tube indirect solar reactor shown in figure 2.2. This work was presented in Abanades *et al.* [2].

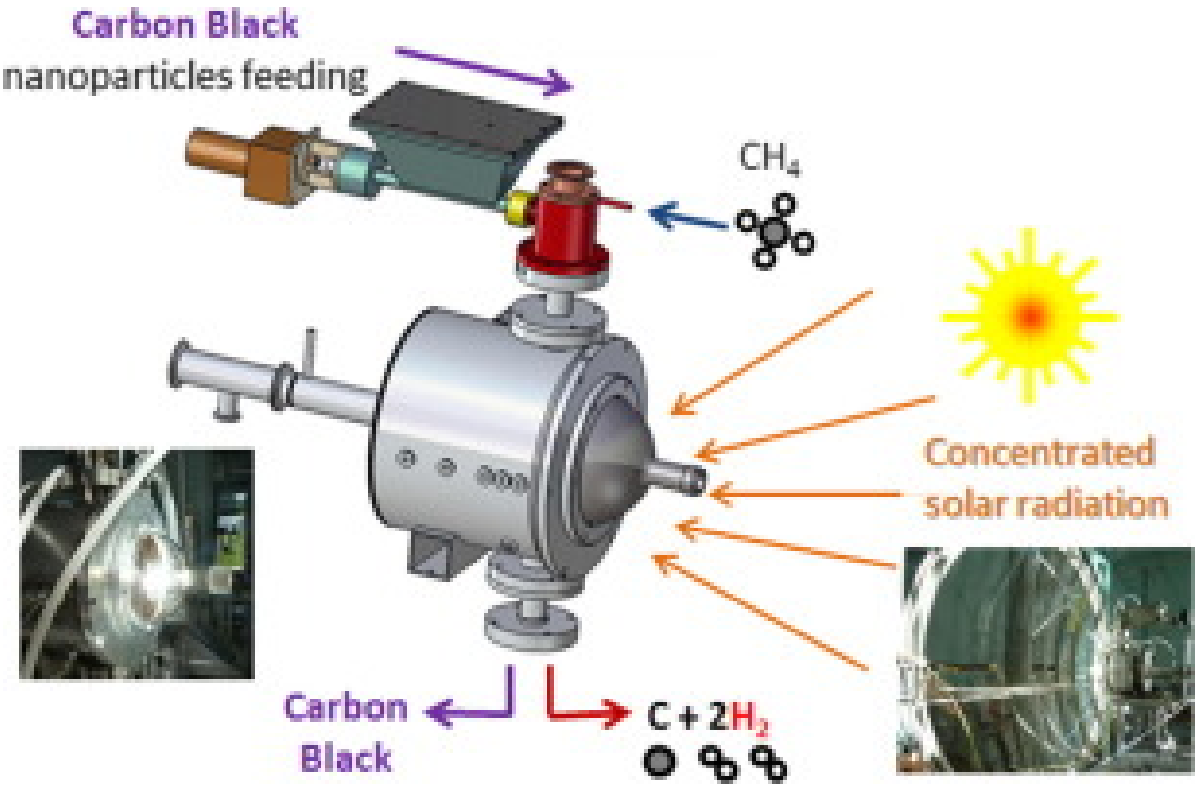

Figure 2.2: A Drop tube solar reactor [Abanades *et al.* [2]]

.

As shown in figure 2.2 the reactor is build of a vertical tube inside a cavity. The concentrated solar radiation is entered into the opaque window. At top of the tube as shown in figure 2.2 is the inlet of the tubes, mixture of methane and carbon black particles are continuously fed so that the reactor can operate continuously. The carbon particles function as catalyst and is expected that the reaction due to this will enhance. To investigate the influence of the carbon particle on the reaction two types of carbon particle were used. The temperature range between $1423 - 1673$ K and the total inlet methane molar fraction was between $10 - 40\%$. Due to small diameter of the reactor the influence of the carbon particle was not so significant for the methane decomposition rate but it is expected when scaling the reactor their will be significant influence of the carbon particles on the reaction product. It was also found that the gas flow rate and the temperature had a significant influence on the decomposition rate of methane.

2.3. Vortex cavity receiver direct solar reactor

Hirsch and Steinfeld have designed a 5 kW vortex flow cavity receiver reactor which is shown in figure 2.3. The concentrated solar radiation is entering through the quartz window into the cavity. At the inlet methane and carbon particle is fed into the reactor. The analysis included coupling to conduction, convection heat transfer and chemical kinetics. During the experiment the effect of particle size and particle loading was examined. It was found that higher particle loading and larger size of the particle will increase the reaction product. Because the efficient absorption will increase and so the temperature of the gas. Another reason is that the reaction surface is also increased Hirsch and Steinfeld [3]. A following up study on the kinetic was maked by Hirsch and Steinfeld [Trommer *et al.* [14]]. A temperature dependence of the reaction rate was describe by using of Arrhenius law with a apparent activation energy in the range $147-162$ kj/mol and a frequency factor in the range $(1.07-7.54)10^6\frac{1}{s}$ was used. The result shows a residence time of $0.3s$ and a methane conversion of 90 % at a reactor temperature of $1500k$. Nesrin Ozalp did a numerical analysis to investigate the influence of the fluid flow inside the vortex flow reactor [Ozalp and JayaKrishna [15]]. The result show that carving in a cavity has significant influence on the flow behavior, however, it has little effect on the outlet temperature.The numerical results also had shown that the radiative heat transfer mechanism is dominant comparing with heat transfer by conduction and convection. Another experimental research of Hirsch and Steinfeld in Hirsch and Steinfeld [16] show that for a reactor temperature in the range of $1000-1600K$ methane and hydrogen conversion of 67 and 33.5 percent was achieved. Kogan developed a tornado flow configuration solar reactor Kogan and Kogan [17]. The tornado flow configuration was chosen to prevent the carbon deposition on the window. Finally a methane conversion of only 28 percent was achieved. It was found that carbon particle was deposited on the wall of the reactor which block the exit and cause clogging.

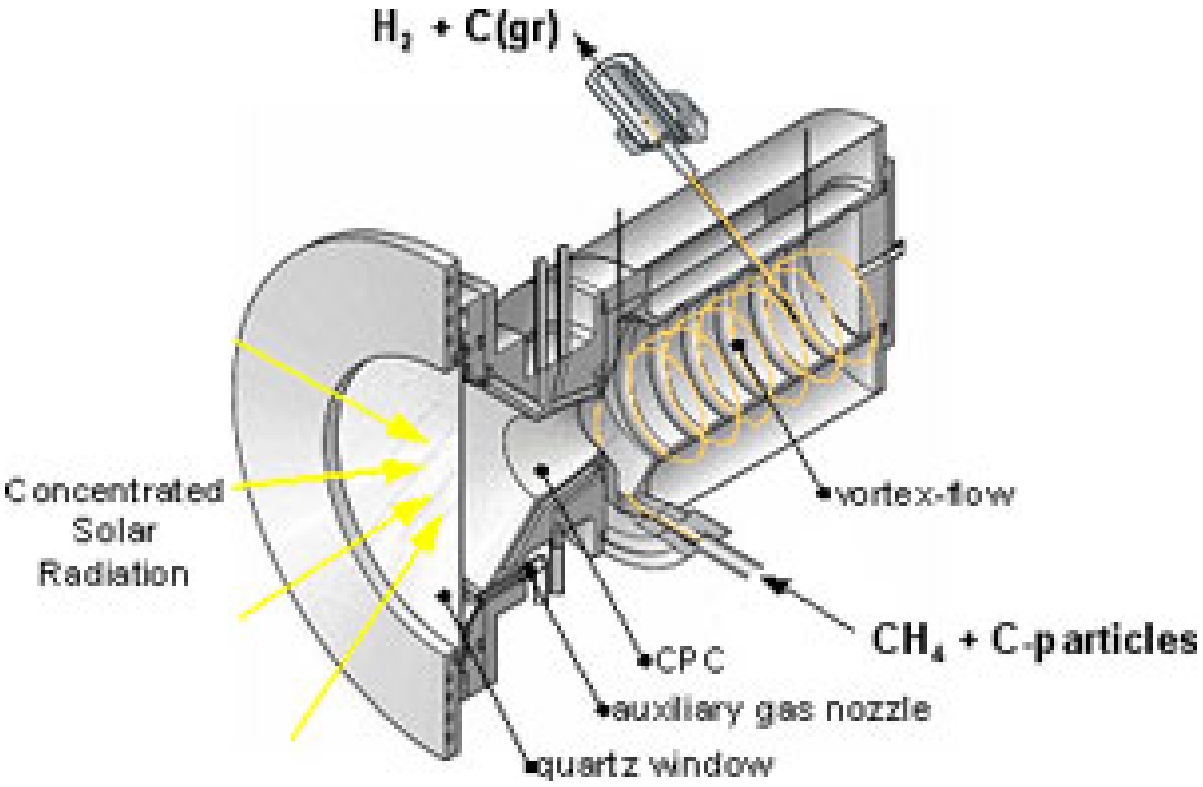

Figure 2.3: vortex-flow direct solar reactor design [Hirsch and Steinfeld [3]].

2.4. Cavity receiver direct solar reactor

Abanades and Flamant developed a cavity receiver solar reactor which is shown in figure 2.4. As can be seen in figure 2.4 a graphite nozzle is place inside a cavity. The concentrated solar radiation is entering brought the window into the graphite nozzle. The graphite nozzle is replaceable so that different nozzle

configurations can be tested. In the experimental research the conversion of methane was strongly dependent on the solar furnace power input, on the geometry of the graphite nozzle, on gas flow rates and on the ratio of inert gas to reactive gas. The chemical conversion of methane to hydrogen and carbon was 95 percent but on the average conversion was in the range $30-95$ percent. In a follow up study theoretical and experimental investigations have been performed Abanades and Flamant [4]. It has shown that the temperature, geometry of the graphite nozzle, gas flow rates and methane molar fraction have a strong influence on the final chemical conversion of methane. The reaction takes place only within a thin region located near a hot graphite wall, where the maximum methane conversion of 98 percent was found at graphite nozzle temperature of $1500K$. Other experimental research showed that the methane conversion and hydrogen yield of 97 and 90 % is reached at a temperature of $1385K$ Abanades and Flamant [18].

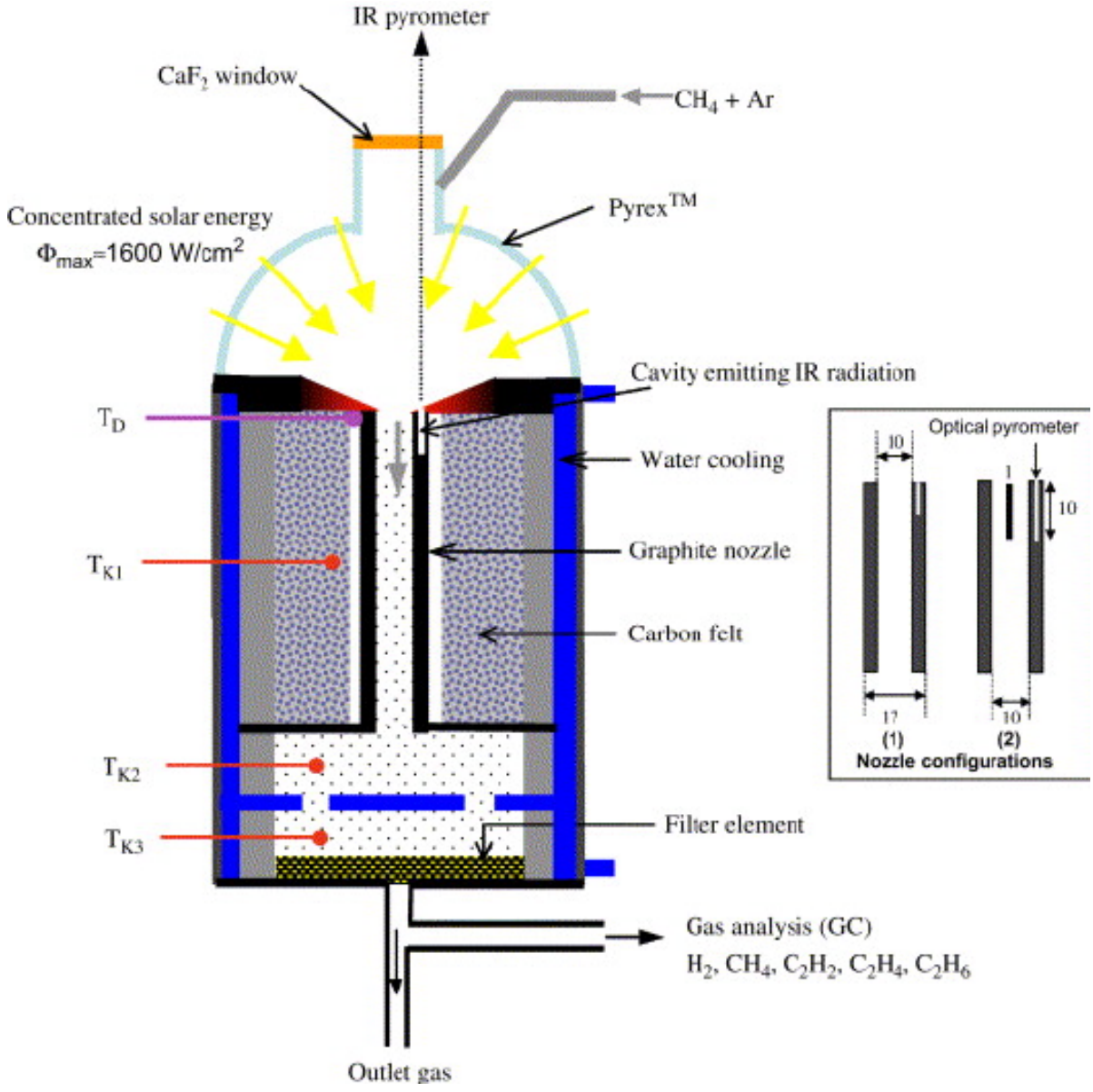

Figure 2.4: Cavity-receiver direct solar reactor design[Abanades and Flamant [4]].

2.5. Aero shield cyclone direct solar reactor

Inspired by the work of Steinfeld and Hirsch an Aero-shield cyclone solar reactor was designed by Krishna and Ozalp [19]. The main problems with the above solar reactor was that after some time

clogging appeared to be a big issue. Due to this the reactor could not be operated continuously. Due to the clogging of the exit port the deposition of carbon particles increased and blocked the heat transfer from the reactor walls in case of indirect heating. The deposition of the carbon particle on the window blocked the window from where the sun radiation enters in cases of direct heating which is known as window darkening. In such case the window heated up further and cracked. In figure 2.5 the aero shield solar reactor design is shown.

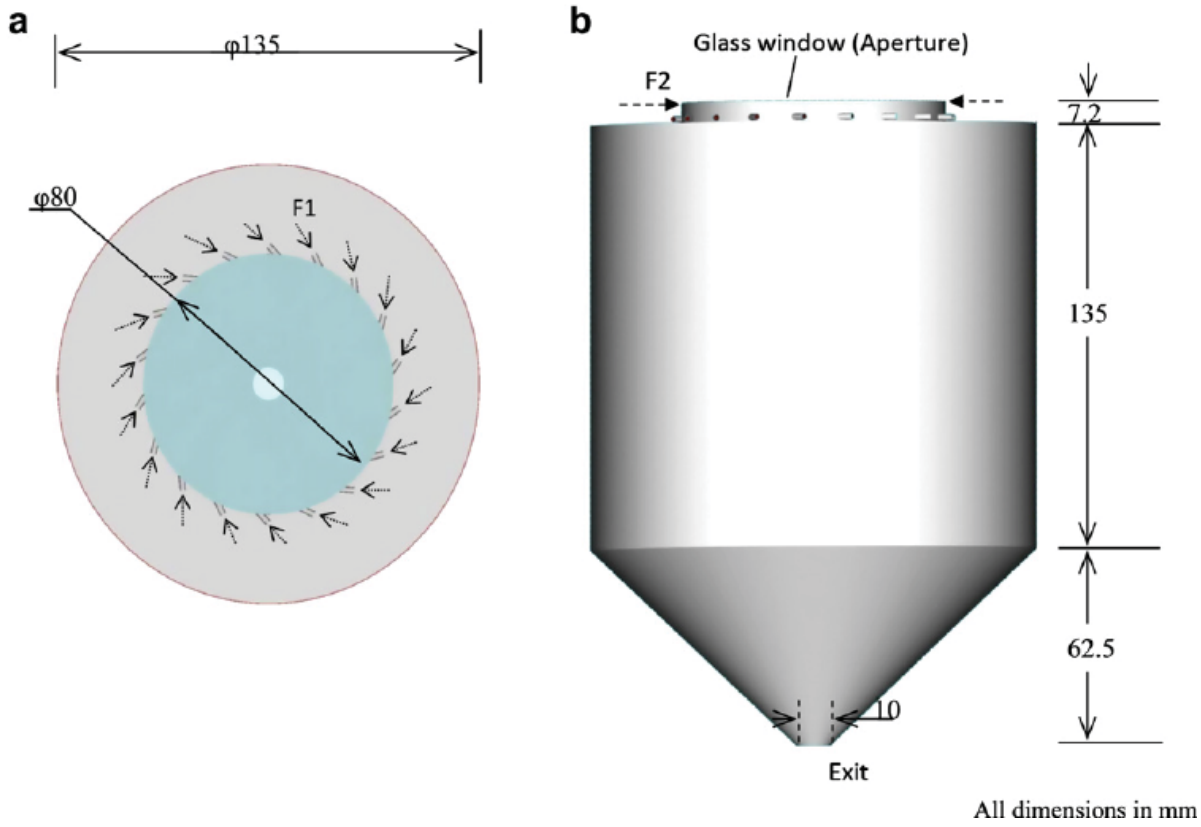

Figure 2.5: Aero-Shield cyclone direct solar reactor design [Ozalp *et al.* [5]].

Argon was injected near the wall and methane and carbon particles were added at the inlet as shown in the figure 2.5. During the simulation of the aero-shield solar reactor, only the fluid dynamics was studied. The focus was more on finding the optimal parameters to avoid carbon particles deposition on the walls and clogging at the exit. To understand the influence of the residence time in the reactor, a computational fluid dynamics study was performed by Ozalp *et al.* [5] and by Shilapuram *et al.* [20]. Experiments were done for a fluid wall aerosol flow reactor by Dahl *et al.* [21] and Wyss *et al.* [22]. To prevent the carbon particles deposition on the walls, argon gas was injected near the wall in order to form a shield for the particles. Result show that when selecting proper gas flow rate and particle the deposition of the carbon particle on the aero shield reactor can be reduced significantly.

2.6. Overview of importants parameter in solar reactor design

In the table 2.1, a summary of all the important reactor parameters is listed for each reactor type. The following parameters are considered : the reactor maximum temperature, methane conversion, hydrogen yield, reactor volume, feedstock, residence time and reactor type.

- The reactor type: By this is mean direct or indirect reactor.
- Catalyst: The reactors can be fed with seed particle carbon black(CB). The catalyst is used to increase the heat transfer from the source to the fluid.
- Reactor volume, flow rate and the residence time: The reactor volume is the volume that the reactor occupies in liter, The volumetric flow rate of methane characterises the throughout. From the reactor volume and the volumetric flow rate the residence time can be calculated.
- The methane conversion, Hydrogen yield and reactor temperature: After the reaction takes place the methane conversion and hydrogen yield can be calculated. The maximum reactor temperature of each reactor is also list in table 2.1.

Parameters	cavity reciever with tube reactor	Drop-tube	vortex-flow reactor	cavity-receiver with nozzle reactor	Aero-shield reactor reactor
Reactor type [–]	indirect	indirect	direct	direct	direct
Katalyst	no	yes [CB]	yes [CB]	no	yes [CB]
Reactor volume [liter]	0.29	0.314	1.57	0.013	2.6
Feedstock volumetric flow rate of methane [liter/min]	1.2	1-3	1.4	0.9	11.11
Residence time [ms]	12-35	38-113	1000	100	1420
Methane conversion [percent]	98	75	67	95	—
Hydrogen Yield [percent]	90	68	33.5	82	—
T-reactor [Kelvin]	1770	1623	1197	1840	2133

Table 2.1: Overview of the performance solar reactors studied in the literature

2.7. Conclusion from literature

In table 2.1 a overview of the different solar reactor designs versus the important parameters is shown. The conversion of methane is highest for the cavity-receiver with a tube reactor based on an indirect concept and lowest for the vortex flow reactor which is based on a direct solar reactor concept. Although the temperature is lower than the cavity receiver with the nozzle reactor and no catalyst is used to enhance the reaction. When the catalyst is used the cavity receiver with nozzle reactor has a higher methane conversion than the drop tube reactor based on an indirect solar reactor. It also appears that the temperature is higher for the cavity receiver with a tube reactor than the drop tube. For the aero shield reactor only non-reacting flow has been studied but it is said in literature that this reactor promised a better control of the clogging problem during operation of the solar reactor. From the data summaries in table 2.1 it is very hard to conclude which reactor is the most promising one and could

be further investigated at industrial scales. Depending on the available data, based on the highest methane conversion, hydrogen yield and simple reactor geometry, the cavity receiver with tube reactor is chosen to perform a computational study .

3

Theory

3.1. Transport equations

This chapter intends to provide fundamental information and present the modeling for the cracking process of methane in a solar reactor. The approach that is employed in this work is the Euler Lagrange method for dispersed multiple phase flow of particles in a laminar gaseous continuum. To understand the results of the modeling part, it is important to understand the physics underlying the solar reactor process. In this chapter the governing equations are non dimensionalized to find out the dominant terms in the equation. The governing equations that are solved are the following:

- Mass conservation equation

$$\frac{\partial \rho}{\partial t} + \frac{\partial (\rho u_i)}{\partial x_i} = 0. \tag{3.1}$$

- Momentum conservation equation

$$\frac{\partial (\rho u_i)}{\partial t} + \frac{\partial (\rho u_i u_j)}{\partial x_j} = -\frac{\partial P}{\partial x_i} + \frac{\partial \tau_{ij}}{\partial x_j}. \tag{3.2}$$

  where τ_{ij} is the viscous stress tensor, defined as follows: $\tau_{ij} = \mu(\frac{\partial u_i}{\partial x_j} + \frac{\partial u_j}{\partial x_i}) - \frac{2}{3}\mu\frac{\partial u_k}{\partial x_k}\delta_{ij}$.

- Species mass conservation equation

$$\frac{\partial (\rho y_k)}{\partial t} + \frac{\partial (\rho u_j y_k)}{\partial x_j} = \frac{\partial}{\partial x_j} J_{k,j} + R_k. \tag{3.3}$$

  where $J_{k,j} = \rho D_{k,g} \frac{\partial y_k}{\partial x_j}$ is the generalised Fick's law.

- Energy conservation equation

$$\frac{\partial (\rho H)}{\partial t} + \frac{\partial (\rho H u_j)}{\partial x_j} = \frac{\partial}{\partial x_j}(\lambda_c \frac{\partial T}{\partial x_j} - \sum_k H_k J_{k,j}) + S_{rad} \tag{3.4}$$

  where $H = H_{thermal} + H_{chemical}$

The variables used in the transport equations are: Density (ρ), velocity (u), time (t), Pressure (P), species mass fraction (y), reaction rate (R), mixture diffusion constant of species $(D_{k,g})$, Enthalpy (H), radiation heat source $(Srad)$, temperature (T) and thermal conductivity (λ_c).

The mass, momentum, species and energy equation as listed above are solved to understand the basic physical phenomena that occur during the methane conversion. However, also the radiative transfer equation (RTE) plays an important role. Radiative heat transfer is explained in section 3.2.

3.2. Dimensionless governing equation

Before starting the analysis of the solar reactor in detail and performing the simulation , it is crucial to understand the transport equations in detail. By non dimensionalizing the governing equations, a more in depth analysis can be performed. The dimensionless numbers help to understand which term is more important and which can be neglected in a specific cases. To make an equation dimensionless, a reference value must be chosen. It will in general be different in different applications.

$$t^* = \frac{tU_o}{D},\ \rho^* = \frac{\rho}{\rho_o},\ T^* = \frac{T}{T_o},\ D^*_{k,g} = \frac{D_{k,g}}{D_{k,g,o}},\ x^* = \frac{x}{D},\ \mu^* = \frac{\mu}{\mu_o},\ u^* = \frac{u}{U_o},\ p^* = \frac{P}{\rho_o U_o^2},\ y^* = \frac{y}{y_o},\ R^*_k = \frac{R_k}{R_o},$$
$$q^*_{rad} = \frac{q_{rad}}{\sigma T_0^4}\quad H^* = \frac{H}{c_{p,o}T_o}\quad c^*_p = \frac{c_p}{c_{p,o}}\quad \lambda^*_c = \frac{\lambda_c}{\lambda_{c,o}}$$

The asterisk $(*)$ represents the non dimensional variables and the indices $(_o)$ represents the reference variables. Beside already mentioned variables, the initial velocity U_o, Dynamic viscosity (μ), Diameter (D), heat capacity (c_p) , x for space coordinate are introduced the radiation source q_{rad}, the chemical heat source S_{chem}, σ is Stefan Boltzmann constant and R_o is a reference value of reaction. Knowing all the above relations, the governing equation can be non dimensionalized. First the mass conservation equation will be made dimensionless as follows:

$$\frac{\rho_o U_o}{D}\frac{\partial \rho^*}{\partial t^*} + \frac{\rho_o U_o}{D}\frac{\partial(\rho^* u_i^*)}{\partial x_i^*} = 0. \tag{3.5}$$

The dimensionless mass conservation equation is divided by $\frac{\rho_o U_o}{D}$ yielding the following equation:

$$\frac{\partial \rho^*}{\partial t^*} + \frac{\partial(\rho^* u_i^*)}{\partial x_i^*} = 0. \tag{3.6}$$

Before making the momentum equation dimensionless, the stress tensor is non dimensionalized as.
$\tau_{ij} = \frac{\mu_o U_o}{D}(\mu^*(\frac{\partial u_i^*}{\partial x_j^*} + \frac{\partial u_j^*}{\partial x_i^*}) - \frac{2}{3}\mu^*\frac{\partial u_k^*}{\partial x_k^*}\delta_{ij})$. where $\tau^*_{ij} = \tau_{ij}\frac{D}{\mu_o U_o}$.
Finally the momentum equation in dimensionless form reads:

$$\frac{\rho_o U_o^2}{D}(\frac{\partial(\rho^* u_i^*)}{\partial t^*} + \frac{\partial(\rho^* u_i^* u_j^*)}{\partial x_j^*}) = -\frac{\rho_o U_o^2}{D}\frac{\partial P*}{\partial x_i^*} + \frac{\mu_o U_o}{D^2}\frac{\partial \tau^*_{ij}}{\partial x_j^*}. \tag{3.7}$$

Dividing the momentum equation by $\frac{\rho_o U_o^2}{D}$ the following is obtained

$$\frac{\partial(\rho^* u_i^*)}{\partial t^*} + \frac{\partial(\rho^* u_i^* u_j^*)}{\partial x_j^*} = -\frac{\partial P^*}{\partial x_i^*} + \frac{\mu_o}{D\rho_o U_o}\frac{\partial \tau^*_{ij}}{\partial x_j^*}. \tag{3.8}$$

The factor $\frac{D\rho_o U_o}{\mu_o}$ is known as the Reynolds number (Re). The Reynolds number has the following physical meaning:

$$Re = \frac{\text{Inertial force}}{\text{Viscous force}}.$$

For low Reynolds number the flow is laminar and for high Reynolds number the flow is turbulent. The transition between laminar and turbulent depends on the flow configuration. So finally the dimensionless momentum equation is rewritten as :

$$\frac{\partial(\rho^* u_i^*)}{\partial t^*} + \frac{\partial(\rho^* u_i^* u_j^*)}{\partial x_j^*} = -\frac{\partial P^*}{\partial x_i^*} + \frac{1}{Re}\frac{\partial \tau^*_{ij}}{\partial x_j^*}. \tag{3.9}$$

The dimensionless form of the species mass conservation is :

$$\frac{\rho_o y_o U_o}{D}\frac{\partial(\rho^* y_k^*)}{\partial t^*} + \frac{\rho_o U_o y_o}{D}\frac{\partial(\rho^* u_j^* y_k^*)}{\partial x_j^*} = \frac{\rho_o D_{k,g,o} y_o}{D^2}\frac{\partial}{\partial x_j^*}(\rho^* D^*_{k,g}\frac{\partial y_k^*}{\partial x_j^*}) + R_o R^*_k. \tag{3.10}$$

Normalizing the species mass conservation equation with the first term on the left side $\frac{\rho_o y_o U_o}{D}$. yields:

$$\frac{(\partial \rho^* y_k^*)}{\partial t^*} + \frac{\partial(\rho^* u_j^* y_k^*)}{\partial x_j^*} = \frac{D_{k,g,o}}{DU_o}\frac{\partial}{\partial x_j^*}(\rho^* D_{k,g}^* \frac{\partial y_k^*}{\partial x_j^*}) + \frac{R_o D}{\rho_o y_o U_o} R_k^*. \tag{3.11}$$

The term on the right hand side $\frac{D_{k,g,o}}{DU_o}$ can be rewritting in the following form as $\frac{D_{k,g,o}}{\nu}\frac{\nu}{DU_o}$ where $\frac{D_{k,g,o}}{\nu}$ is known as the inverse of the Schmidt number and the latter ($\frac{\nu}{DU_o}$) is already mentioned. The Schmidt numbers represents the following:

$$Sc = \frac{\text{viscous diffusion rate}}{\text{molecular(mass) diffusion rate}}.$$

The term $\frac{R_o D}{\rho_o U_o y_o}$ is known as Damkohler number (D_a). Damkohler number has the meaning :

$$Da = \frac{\text{reaction rate}}{\text{convective mass transfer rate}}.$$

The dimensionless species mass transfer equation is then:

$$\frac{\partial(\rho^* y_k^*)}{\partial t^*} + \frac{\partial(\rho^* u_j^* y_k^*)}{\partial x_j^*} = \frac{1}{ScRe}\frac{\partial}{\partial x_j^*}(\rho^* D_{k,g}^* \frac{\partial y_k^*}{\partial x_j^*}) + DaR_k^*. \tag{3.12}$$

Finally the energy conservation equation is non dimensionalized.
To make the energy equation dimensionless first the heat source contribution by radiation is analysed.

$$S_{rad} = \frac{\partial q_{rad}}{\partial x_j} = \frac{\sigma T_o^4}{D}\frac{\partial q_{rad}^*}{\partial x_j^*}$$

Then the energy equation becomes:

$$\frac{\rho_o H_o U_o}{D}\frac{\partial(\rho^* H^*)}{\partial t^*} + \frac{\rho_o H_o U_o}{D}\frac{\partial(\rho^* H^* u_j^*)}{\partial x_j^*} = \frac{1}{D}(\frac{\partial}{\partial x_j^*}(\frac{\lambda_{c,o} T_o}{D}\lambda_c^*\frac{\partial T^*}{\partial x_j^*} - \sum_k H_o H_k^*(-\frac{\rho_o D_{k,g,o} y_o}{D}\rho^* D_{k,g}^*\frac{\partial y_k^*}{\partial x_j^*}))) + \frac{\sigma T_o^4}{D}\frac{\partial q_{rad}^*}{\partial x_j^*}. \tag{3.13}$$

where $H_o = c_{p.o} T_o$.
Dividing the whole equation by $\frac{\rho_o H_o U_o}{D}$:

$$\frac{\partial(\rho^* H^*)}{\partial t^*} + \frac{\partial(\rho^* H^* u_j^*)}{\partial x_j^*} = (\frac{\partial}{\partial x_j^*}(\frac{\lambda_{c,o} T_o}{DU_o H_o \rho_o}\lambda_c^*\frac{\partial T^*}{\partial x_j *} - \sum_k H_k^*(-\frac{D_{k,g,o} y_o}{DU_o}\rho^* D_{k,g}^*\frac{\partial y_k^*}{\partial x_j^*}))) + \frac{\sigma T_o^4}{\rho_o H_o U_o}\frac{\partial q_{rad}^*}{\partial x_j^*} \tag{3.14}$$

In the dimensionless equation the following term is found

$$\frac{\lambda_{c,o} T_o}{DU_o H_o \rho_o} = \frac{\lambda_{c,o}}{c_{p,o}\mu_o}\frac{\mu_o}{DU_o\rho_0}.$$

Where $\frac{\lambda_{c,o}}{c_{p,o}\mu_o}$ is the inverse of the Prandtl number ($\frac{1}{Pr}$). The Prandtl number (Pr) is defined as follow:

$$Pr = \frac{\text{viscous dissipation rate}}{\text{thermal diffusion rate}}$$

and the Reynolds and Schmidt numbers are already mentioned. A new term $\frac{\sigma T_o^4}{\rho_o H_o U_o}$ can be rewritten as follow: $\frac{\sigma T_o^3 D}{\lambda_{c,o}}$, $\frac{\mu_o}{\rho U_o D}$ and $\frac{\lambda_{c,o}}{c_{p,o}\mu_o}$. The first one is the inverse of the Planck number($\frac{1}{Pl}$), the second and third one was already explained above. The Planck number can also defined differently with $h = c_{p(T_o - T_{ref})}$ and $q_{rad}^* = \frac{q_{rad}}{\sigma(T_0^4 - T_{ref}^4)}$ as follow: $\frac{\lambda_{c,o}(T_o - T_{ref})}{\sigma D(T_0^4 - T_{ref}^4)}$. Planck number (Pl) has the meaning:

$$Pl = \frac{\text{conductive heat transfer rate}}{\text{radiative heat transfer rate}}.$$

Finally the energy conservation equation can be rewritten in dimensionless form as follows:

$$\frac{\partial(\rho^* H^*)}{\partial t^*} + \frac{\partial(\rho^* H^* u_j^*)}{\partial x_j^*} = (\frac{\partial}{\partial x_j^*}(\frac{1}{PrRe}\lambda_c^* \frac{\partial T^*}{\partial x_j^*} - \sum_k H_k^*(-\frac{y_o}{ScRe}\rho^* D_{k,g}^* \frac{\partial y_k^*}{\partial x_j^*}))) + \frac{1}{PlRePr}\frac{\partial q_{rad}^*}{\partial x_j^*}. \tag{3.15}$$

In table 3.1 a summary of all the dimensionless number is given.

Name of dimensionless number	abbreviation	definitions
Reynolds	Re	$\frac{D\rho_o U_o}{\mu_o}$
Schmidt	Sc	$\frac{\nu}{D_{k,g,o}}$
Damkohler	Da	$\frac{R_o D}{\rho_o U_o y_o}$
Prandtl	Pr	$\frac{c_{p,o}\mu_o}{\lambda_{c,o}}$
Planck 1	Pl	$\frac{\lambda_{c,o}}{\sigma T_o^3 D}$
Planck 2	Pl	$\frac{\lambda_{c,o}(T_o - T_{ref})}{\sigma D(T_o^4 - T_{ref}^4)}$

Table 3.1: Summary of dimensionless numbers

3.3. Radiation heat transfer

The three heat transfer mechanisms are conduction, convection and radiation. In systems that operate at high temperature, the radiative heat transfer mechanics is dominant over convection and conduction. In a solar reactor the sun light most often is concentrate by using of a concentrator. A concentrator is a system of mirrors or lenses to concentrate the sunlight or solar thermal energy coming from a large area, onto a small area. In this way the flux of radiative energy is increased. A wave traveling in a medium is affected in terms of direction, intensity and wavelength. During the interaction of the radiative wave and the working medium, photons are absorbed, reflected, transmitted and sometimes emitted by the medium as shown in figure 3.1.

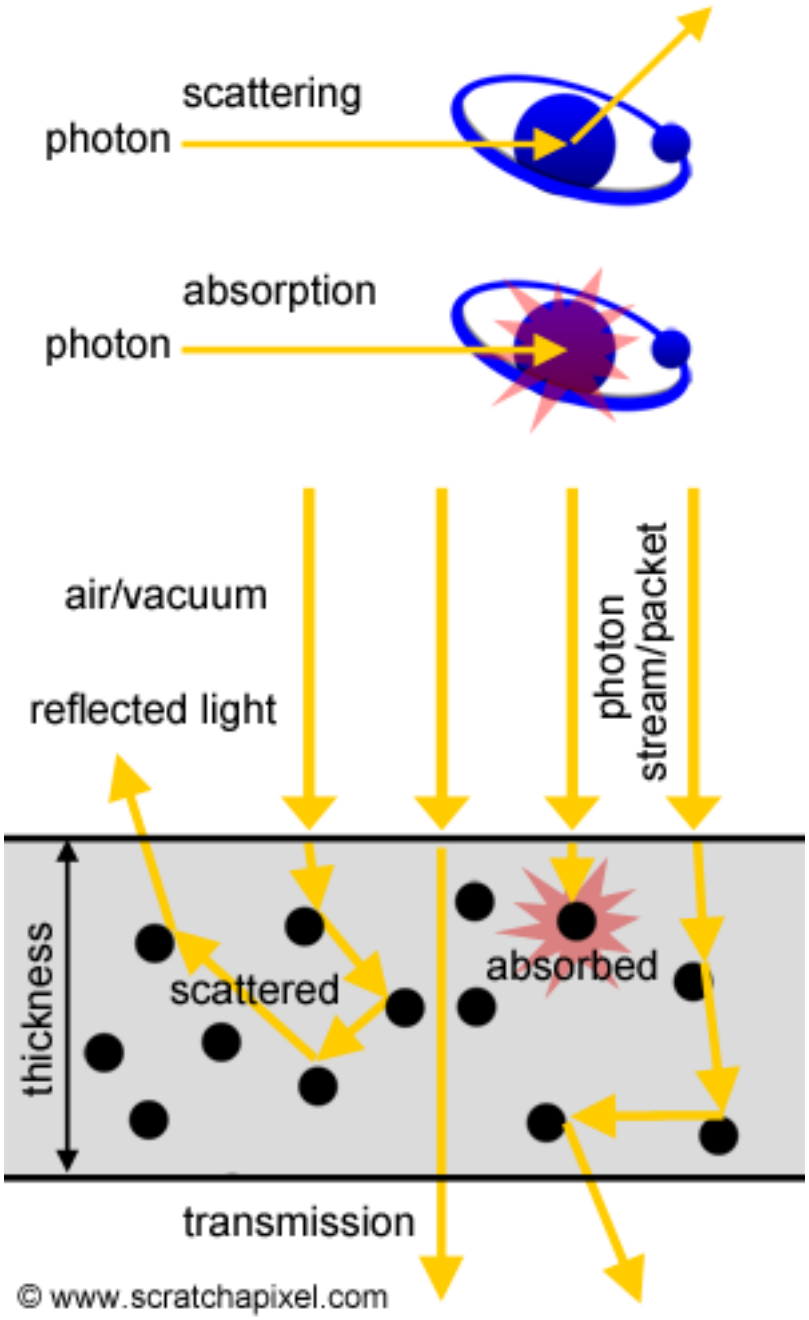

Figure 3.1: Absorbed,reflected, transmitted and scattered by a medium

When radiation is absorbed or scattered in a medium, the medium is known as participating media.The interaction of radiation with medium is determined by the optical properties of the medium. The optical properties are dependent on the wavelength. Depending how the radiation wave interact with the medium, it can be observed that some medium absorbed a lot of the radiation or scatter almost all the incoming radiation. Radiation can be describe as the emission or transmission of energy in the form of wave or particles through wave or though a material medium. The power transferred per unit area, where the area is measured on the plane perpendicular to the direction of propagation of the energy it is known as the intensity. When the wave interact with the medium part of the energy can be scatter in any direction. When wave is scattered in the opposite direction as the incoming radiation it is known as back scattering and when it scatter in the same direction as the incoming radiation it is known as forward scattering. In figure 3.2 is shown how scattering by particles can result by the combined effect of diffraction, refraction and reflection.

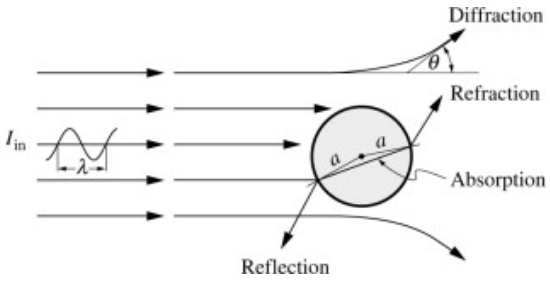

Figure 3.2: Interaction of electromagnetic wave with a particle.Taken from radiative heat transfer[Modest [6]]

Figure 3.2 Interaction of electromagnetic wave with small particle. Taken from Radiative Heat Transfer **??**(Michael F.Modest(third edition)

3.3.1. Black body spectral intensity

The black body is an idealized radiative body that in one hand absorbs all the incident radiation and on the other hand emits the maximum possible radiation. The radiation that is emitted by a black body (black body emissive power) can be described by Planck's law as follow:

$$e_{\lambda,b}(\lambda,T) = \frac{2\pi h c_o^2}{n^2\lambda^5(exp(\frac{hc_0}{n\lambda k_B T}) - 1)} \tag{3.16}$$

Where h is the Planck constant, c_o the speed of light in a vacuum , k_B is the boltzman constant, λ is the wavelength, T is the temperature and n is refractive index of the gas near the black body.
As visible from the Planck's law the amount of energy depends on the wave length and the temperature. The black body spectral intensity is defined as follows:

$$I_{b\lambda}(\lambda,T) = \frac{e_{\lambda,b}(\lambda,T)}{\pi} \tag{3.17}$$

The unit of the emitted radiation are per unit area of emitting surface, per unit solid angle and per unit wave length. The spectral intensity is shown in figure 3.3 as function of wavelength and temperature. The peak of intensity reduces in magnitude and shifts to larger wavelength with decreasing temperature. The Planck's law is derived from quantum mechanics. A radiation law using classical physics does not agree with measurements.(also in figure 3.3)

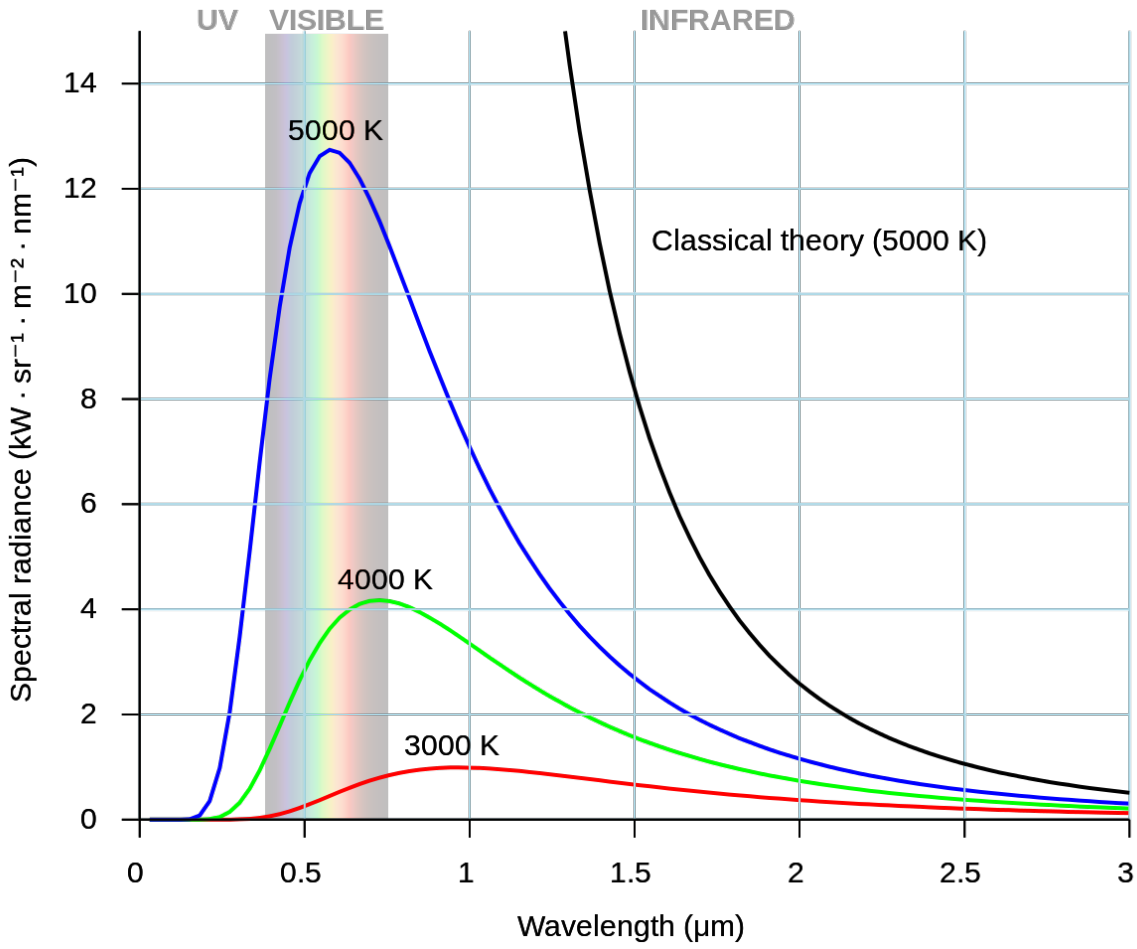

Figure 3.3: Spectral intensity as function of wavelength and temperature

3.3.2. Radiative heat transfer equation

In case of disperse multiple phase flow as participate media the radiation transfer equation is formulated as follows accounting for the contributions of both the solid and gas phases. The variation of spectral radiation intensity along a path in the two phase medium is obtained by adding up the contribution terms for absorption, emission and scattering :

$$dI_\lambda = dI_{\lambda,abs} + dI_{\lambda,emit} + dI_{\lambda,scat} + dI_{\lambda,isc}. \tag{3.18}$$

where the indeces abs, emit, scat stand for absorption, emitting, scattering and isc for incoming scattering.
The above equation of the spectral radiation intensity can be rewritten as follow:

$$dI_\lambda = -\kappa_\lambda I_\lambda(\hat{s})ds + dI_{\lambda,emi,g} + dI_{\lambda,emit,s} - \sigma_{s\lambda} I_\lambda(\hat{s})ds + \frac{\sigma_{s\lambda}}{4\pi}\int_{4\pi} I_\lambda(\hat{s_i})\Phi_{\lambda,s}(\hat{s_i},\hat{s})d\Omega_i ds. \tag{3.19}$$

where $\kappa_\lambda = \kappa_{\lambda,g} + \kappa_{\lambda,s}$ is the absorption coefficient of the solid and gases phase, $I_{b\lambda}$ is the spectral black body intensity, $\sigma_{s\lambda}$ is the scattering coefficient, $\Phi_{\lambda,s}(\hat{s_i},\hat{s})$ is the scattering phase function where i is the incoming direction and $\hat{s}$ is beam travelling path and $d\Omega = sin\theta d\theta d\psi$.

3.3.3. Absorption

When the medium is consists of multiple phase each phase contribute to the overall absorption coefficient. The absorption coefficient of particles is calculated by taking into account the volume fraction. Therefore the absorption coefficient can be formulated as follow:

$$dI_{\lambda,abs} = -\kappa_{\lambda,s} I_\lambda ds - \kappa_{\lambda,g} I_\lambda ds = -\kappa_\lambda I_\lambda ds. \tag{3.20}$$

The contribution of each phase j can then be given as:

$$dI_{\lambda,abs,j} = \frac{-\kappa_{\lambda,j} I_\lambda ds}{-\kappa_\lambda I_\lambda ds} dI_{\lambda,abs} = \frac{\kappa_{\lambda,j}}{\kappa_\lambda} dI_{\lambda,abs}. \tag{3.21}$$

3.3.4. Emission

In analogy to the absorbed intensity, the emitted intensities involve contribution from both the solid and gas phases. The emitted intensities can depend on different temperatures so they must be treated differently.

$$dI_{\lambda,emit} = \kappa_{b\lambda,s} I_{b\lambda}(T_s) ds + \kappa_{b\lambda,g} I_{b\lambda}(T_g) ds. \tag{3.22}$$

Where T_s and T_g are temperature of solid and gas. As defined for the absorption case, a similar expression can be derived for the emission part from each phase j as follows:

$$dI_{\lambda,emit,j} = \frac{\kappa_{\lambda,j} I_{b\lambda}(T_j)}{\kappa_{\lambda,s} I_{b\lambda}(T_s) + \kappa_{\lambda,g} I_{b\lambda}(T_g)} dI_{\lambda,emit}. \tag{3.23}$$

3.3.5. Scattering

For the scattered intensity the equation for a two phase medium becomes:

$$dI_{\lambda,sc} = -\sigma_{s\lambda,s} I_\lambda ds - \sigma_{s\lambda,g} I_\lambda ds = -\sigma_{s\lambda,s} I_\lambda ds = -\sigma_{s\lambda} I_\lambda ds. \tag{3.24}$$

The scattering contribution from each phase it is completely in analogy to the absorption definitions. The spectral scattering coefficient is defined as follows:$\sigma_{s\lambda} = \sigma_{s\lambda,s} + \sigma_{s\lambda,g}$. However in the case of interest to us scattering from the gas phase is negligible in comparison with the scattering from the particles.

$$dI_{\lambda,sc} \approx dI_{\lambda,sc,s}. \tag{3.25}$$

Also the incoming scattering depends only on the scattering coefficient of the particles. The expression for the incoming scattering is:

$$dI_{\lambda.isc} \approx \frac{\sigma_{s\lambda,s}}{4\pi} \int_{4\pi} I_\lambda(\hat{s}_i) \Phi_{\lambda,s}(\hat{s}_i, \hat{s}) d\Omega_i ds. \tag{3.26}$$

3.4. Radiative properties of particle

3.4.1. Assumption for particles

The parameters governing the absorption and scattering for particle are:

- The shape of the particle is assumed spherical.
- The particle size parameter(ξ):

$$\xi = \frac{\pi d_p}{\lambda} \tag{3.27}$$

  where d_p is the particle diameter and λ is the wave length.

- The clearance between particles: It is assumed that the distance between the particles is large enough that the scattering can be assumed to be independent. Therefore, the scattering from one particle is not affected by the presence of surrounding particles. In figure 3.4 the scattering map as function of the particle size parameter and volume fraction is plotted.
- The volume fraction of particles f_v.

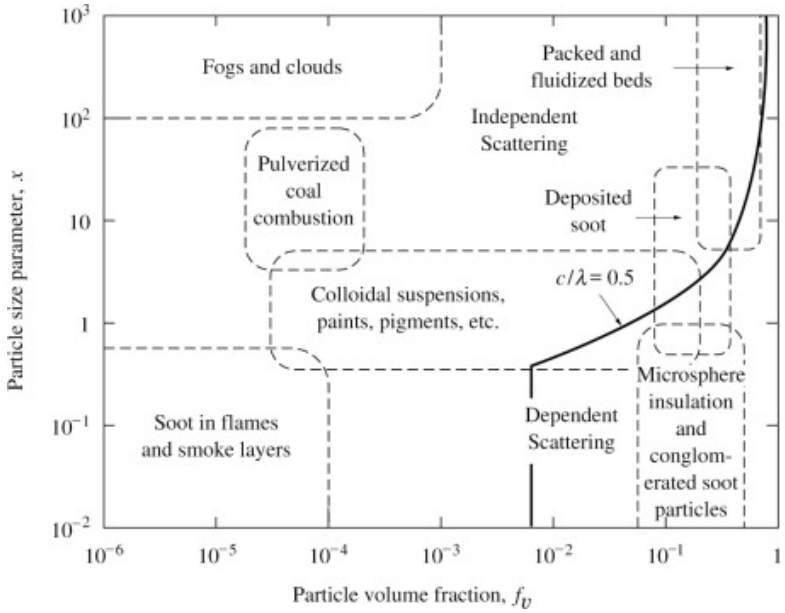

Figure 3.4: Scattering map function of ξ and f_v. [Modest [6]]

In this work the particle size parameter is not exceeding 1 and for the volume fraction is lower than 10^{-4}. Therefore the assumption of independent scattering can be justified.

3.4.2. Mie theory

The Mie theory is valid over a wide range of particle size parameter and will be used to calculate the amount of incoming radiation that is absorbed or scattered by the particle. Therefore, the Mie theory will be explained below in this section.

$$\sigma_\lambda = A_p N_p Q_{sca,\lambda} = \frac{\pi d_p^2}{4}\frac{3}{2}\frac{f_v}{V_p}Q_{sca,\lambda} = \frac{3}{2}\frac{f_v}{d_p}Q_{sca,\lambda} \tag{3.28}$$

$$\kappa_\lambda = A_p N_p Q_{abs,\lambda} = \frac{\pi d_p^2}{4}\frac{3}{2}\frac{f_v}{V_p}Q_{abs,\lambda} = \frac{3}{2}\frac{f_v}{d_p}Q_{abs,\lambda} \tag{3.29}$$

In the above equation $Q_{abs,\lambda}$ and $Q_{scat,\lambda}$ is the absorption efficiency and scattering efficiency, A_p, V_p, and N_p stand for particle projected area, particle volume and number of particle per volume. The absorption and scattering efficiencies are the ratio of the absorption and scattering cross section to the geometrical cross section, respectively and are defined as follow:

$$Q_{abs,\lambda} = \frac{C_{abs,\lambda}}{A_p} \tag{3.30}$$

$$Q_{scat,\lambda} = \frac{C_{sca,\lambda}}{A_p} \tag{3.31}$$

The absorption and scattering efficiencies depend on the incoming wavelength and on the particle size. Mie theory solves the scattering and absorption efficiencies by solving the electromagnetic wave incident on a particle accompanied by an abruptly changing refractive index. The following step needs to be made for calculating the efficiencies:

$$Q_{abs,\lambda} = \frac{2}{\xi^2}\sum_{i=1}^{\infty}(2n-1)Re(|\,a_n\,|^2 + |\,b_n\,|^2) \tag{3.32}$$

$$Q_{scat,\lambda} = \frac{2}{\xi^2}\sum_{i=1}^{\infty}(2n-1)(|\,a_n\,|^2 + |\,b_n\,|^2) \tag{3.33}$$

where the coefficients a_n and b_n are defined as follow:

$$a_n = \frac{m * \psi_n(m\xi)\psi_n'(\xi) - \psi_n(\xi)\psi_n'(m\xi)}{m * \psi_n(m\xi)\chi_n'(\xi) - \chi_n(\xi)\psi_n'(m\xi)} \tag{3.34}$$

$$b_n = \frac{\psi_n(m\xi)\psi_n'(\xi) - m\psi_n(\xi)\psi_n'(m\xi)}{\psi_n(m\xi)\chi_n'(\xi) - m\chi_n(\xi)\psi_n'(m\xi)} \tag{3.35}$$

ψ_n and χ_n are the Ricatti-Bessel functions is while the prime indicates their derivatives. The relative refractive index m is given by

$$m = \frac{n_p + ik_p}{n_{medium} + ik_{medium}} \tag{3.36}$$

The relative refraction index ratio (m) is define as the ratio of complex refractive index of the particle and the complex refractive index of the gas. The complex refractive index is composed of a real part n which is called refractive index and a imaginary part k which is called mass attenuation. The complex refractive index depends on the material properties and on the wavelength.
When the particle size parameter is $\xi << 1$, Rayleigh scattering can be applied and when $\xi >> 1$ geometric optical theory can be used. In this work the particle size parameter is around one, therefore the Mie theory will be used. In figure 3.5 the different region are shown where the Rayleigh, Mie or optical theory can best be used to calculate the absorption and scattering coefficient.

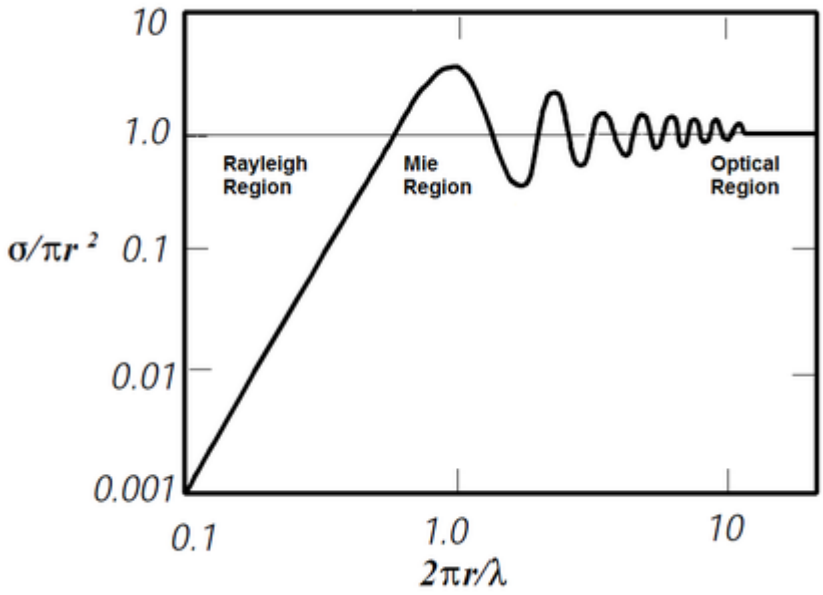

Figure 3.5: shows how the region of the Rayleigh, Mie and optical scattering as function of particle size parameter[Modest [6]]

3.4.3. Optical thickness

Another crucial factor is the optical thickness (τ) which is defined as follow:

$$\tau_\lambda(s) = \int_0^s \kappa_\lambda(s)ds \tag{3.37}$$

where $\kappa_\lambda(s)$ is the absorption coefficient a position s along the path. The optical thickness (τ_λ) is the integral of the absorption coefficient along the path (s) on an individual ray of light. When the optical thickness is high the medium can be referred as optically thick. When the optical thickness is low the medium can be defined as optically thin. In the solar reactor design the desired optical condition is

that all the heat is absorbed by the medium. When the condition is optical thick only a small layer at the side where radiation enters is heat up and when the condition is optical thin the radiation reaches the opposite side of the reactor. These condition must be avoided. Therefore, the optical thickness must be optimized in order to find optimum value to improve the design and performance of the solar reactor.

3.5. Chemical Kinetics

For the cracking of methane into hydrogen and carbon particle it is very important to understand the chemical kinetics. Methane is converted in reality in multiple step and this produces also other byproducts. Depending on the chemical kinetics the reaction can be controlled to get the desire result. The reaction speed depends on the kinetics parameters. so for the methane cracking reaction:

$$CH_4(g) \rightarrow C_s + 2H_2(g) \tag{3.38}$$

the chemical kinetic rate have to be considered. The chemical kinetics are complex since the reaction rate r_{CH4} depends on particle surface and catalytic activity which greatly differ between the type of carbon. In the master thesis work of Rubino [[9]] the following reaction rate was proposed for the one step reaction of methane.

$$r_{CH4} = \frac{k_o}{k_{exp}^{-}} exp(\frac{-E_a}{RT}) \hat{\rho_{CH4}} \tag{3.39}$$

Where $k_o = 1.0610^{-}6\frac{1}{s}$, $k_{exp}^{-} = 8.84\frac{mol}{m^3}$, $E_a = 147\frac{kj}{mol}$ and $\hat{\rho_{CH4}}$ is the partial molar density. k_{exp} is a normalisation deduced from calibration with experiment. The kinetic rate is based on the work of Maag [[9]]. This methane reaction rate will be used in this work.

From the Arrhenius type rate law the following reaction time scale can be obtained:

$$\tau = \frac{1}{\frac{k_o}{k_{exp}^{-}} exp(\frac{-E_a}{RT}) \hat{\rho_{CH4}}} \tag{3.40}$$

From the methane reaction equation the carbon particle reaction rate and hydrogen reaction rate relation can be derived as follows:

$$r_{carbon} = -r_{CH4} \tag{3.41}$$

and

$$r_{H_2} = 2r_{carbon} \tag{3.42}$$

where the reaction rate of methane is negative because methane is consumed. On the contrary, the reaction rates of carbon and hydrogen gas are positive because these are produced during the reaction.

The methane and hydrogen conversion is defined by the following formulas:

$$X_{ch4} = \frac{F_{ch4,in} - F_{ch4,out}}{F_{ch4,in}} \tag{3.43}$$

$$X_{h2} = \frac{F_{h2,out}}{2 * F_{ch4,in}} \tag{3.44}$$

where F stand for the molar fraction. The molar fraction is calculated by using the report type mass weighted average formula in fluent. where θ is the field variable (F).

$$\frac{\int \theta \rho |\vec{v} d\vec{A}|}{\int \rho |\vec{v} d\vec{A}} \tag{3.45}$$

3.5.1. Reaction rate for single particle

Assuming that all methane conversion take place at the surface of the particles, the reaction rate in equation 3.39 can be transformed to reaction rate for a given particle concentration. If the particles are assumed to have the same size the reaction rate per particle can be obtained [Rubino [9]]. The reaction rate law is specified in term of mass concentration of carbon particles in the total volume as follows.

$$\frac{d\rho_s}{dt} = \frac{\rho_s}{\tau} \tag{3.46}$$

ρ_s is not the density of solids carbon but the particle density of carbon in the mixture and τ the reaction time scale.

The particle density ρ_s is defined as follow:

$$\rho_s = \frac{N_p V_p}{V} \rho_C V = V_g + V_s \tag{3.47}$$

The total volume V is the sum of fluid and solid particle volume.

$$V = V_g + V_s \tag{3.48}$$

Then the total variation of particles mass (m_s) in the gas mixture will be given as:

$$\frac{dm_s}{dt} = \frac{d(V\rho_s)}{dt} = \rho_s \frac{dV}{dt} + V\frac{d\rho_s}{dt} \tag{3.49}$$

Assuming that the volume taken by the two phase mixture is not changing $\frac{dV}{dt} = 0$ and . therefore:

$$\frac{dm_s}{dt} = \frac{V\rho_s}{\tau} \tag{3.50}$$

Using the above equation the total variation in mass of the particles in the gas mixture is:

$$\frac{dm_s}{dt} = \frac{N_p V_p \rho_C}{\tau} \tag{3.51}$$

thus the equation for single particle reaction can be rewritten as:

$$\frac{dm_s}{dt} = V_p r_p \tag{3.52}$$

where

$$r_p = \frac{\rho_c}{\tau} = r_{c,p} \tag{3.53}$$

In equation 3.53 the reaction rate of single particle is given. The reaction rate is dependent on the properties and geometries of a single particle as well as on the surrounding condition of the gas phase. Equation 3.53 can be used in order to derive the reaction rates of methane and hydrogen gas. The reaction rate contribution of a single particle to the gas phase for methane is:

$$r_{ch4} = -\frac{M_{ch4}}{M_c} r_p \tag{3.54}$$

and for hydrogen:

$$r_{h2} = -\frac{2M_{h2}}{M_c} r_p \tag{3.55}$$

Equation 3.54 and 3.55 express conservation of mass [Rubino [9]]. Where M_{ch4}, M_c and M_{h2} is the molar mass of methane, carbon particles and hydrogen.

4

Setup of computational model

4.1. Problem description

As indicated in chapter 2 several solar reactor concepts has been designed and tested. During the literature study it was not clear which design was the most promising for building on industrial scale. We decided perform a simple computational fluid dynamics (CFD) analyses on the tube reactor concept. The decision to used the tube reactor was taken because of availability of open literature on the reactor and because of the simple geometry of the tube. Because of the simplicity of the geometry the role of the dimensionless numbers can be derive easily. To perform a CFD analyses several model simplification of the real reactor have to be introduced in order to reduce the complexity of the system. One of the simplification is that the analyses will be done on a single two dimensional tube indeed of a bundle of tubes which is the case in real solar reactor.

4.2. software

To understand and analyze the process inside the solar reactor a computational fluid dynamics analysis is performed on a tubular solar reactor. ANSYS fluent software is used. ANSYS Fluent is a general propose computational fluid dynamics (CFD) tool. "Fluent includes well-validated physical modeling capabilities to deliver fast, accurate results across the widest range of CFD and multiphysics applications. ANSYS Fluent software contains the broad physical modeling capabilities needed to model flow, turbulence, heat transfer, and reactions for industrial applications ranging from air flow over an aircraft wing to combustion in a furnace, from bubble columns to oil platforms, from blood flow to semiconductor manufacturing, and from clean room design to waste water treatment plants. Fluent covers a broad reach, including special models with capabilities to model in cylinder combustion, aero acoustics, turbo machinery and multiple phase systems" Manual [23].

It is possible to implement user defined function (UDF) in Ansys fluent. The user defined functions allow users to customize fluent so that significantly enhance its capabilities to specific project requirements. In the user defined function manual that is provide by fluent are present many inbuild functions that can be used to manipulate variables for specific applications[Fluent [24]. In this work three new user defined function are written. The first one is written for the mean planck absorption coefficient of the methane gas (mixture). The second user defined function is used for the time evolution of particle properties. In this user defined function each particle is called and reaction is perform on the surface. The carbon that is produced is added to the surface of the particle and the new diameter is calculated. The last user defined function is written for the absorption coefficient of the particles. Depending on each particle diameter and temperature a scattering efficiency and absorption efficiency value is obtained.

The Mie theory software is used separately to generate a table for the scattering efficiency and absorption efficiency. When the particles are included in the simulation, fluent calculates an equivalent

absorption coefficient of the particle cloud.

$$a_p = \lim_{V \to 0} \sum_{n=1}^{N} Q_{abs} \frac{A_{pn}}{V} \tag{4.1}$$

where a_p is the equivalent absorption coefficient of the particle, Q_{pn} is the absorption efficiency, A_{abs} is the projected area of a particle and is calculated as follows $\frac{d^2\pi}{4}$, where d is the diameter of particle and V is the volume of the cell.

and similarly for the scatting coefficient the following formula is used.

$$\sigma_p = \lim_{V \to 0} \sum_{n=1}^{N} (Q_{sca}) \frac{A_{pn}}{V} \tag{4.2}$$

where Q_{sca} is the scattering efficiency.

To simulate the solar reactor, an Eulerian-Lagrangian method is chosen. The fluid is modeled with an Eulerian frame of reference and the particles are modeled in a Lagrangian frame of reference. Using this Eulerian frame of reference the velocity, temperature and species behavior are determined. For the particles, the position, velocity and temperature behavior are determined in Lagrangian frame of reference where each particle is followed separately. In this way the fluid and particle properties are calculated by using the radiation model. After the temperature of the system is known the UDF are used to calculate the methane reaction of the surface and the new particle diameter is calculated. The produced hydrogen and consumed methane is given back as a source or sink in the system.

4.2.1. Geometry

The reactor geometry is the same as used by Caliot et al. The tube has a diameter (d) of 15 mm and length (L) of 600 mm. A gas mixture of argon, methane and particles are injected at the inlet of the tube. In figure 4.1 the cross section of the axis symmetric geometry is shown as it implemented in ANSYS fluent. In this figure 4.1 half of the longitudinal tube geometry is shown.

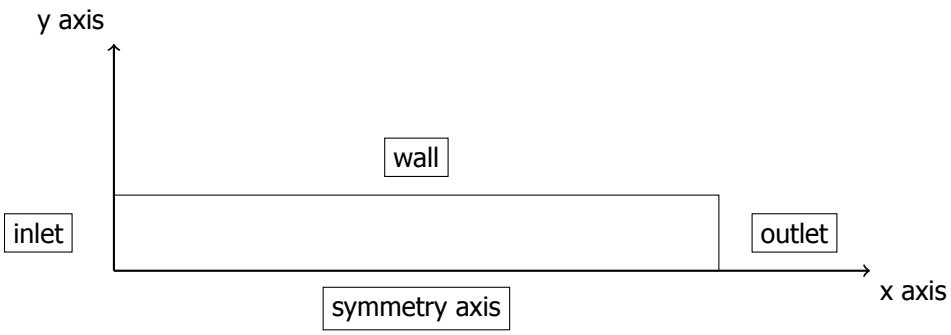

Figure 4.1: 2D geometry sketch of the tube. Where the symmetry is located at the center of the tube.

The mesh of the geometry is generated by dividing the geometry in horizontal direction into 50 cells and in vertical direction into 100 cells which is shown in figure 4.2.

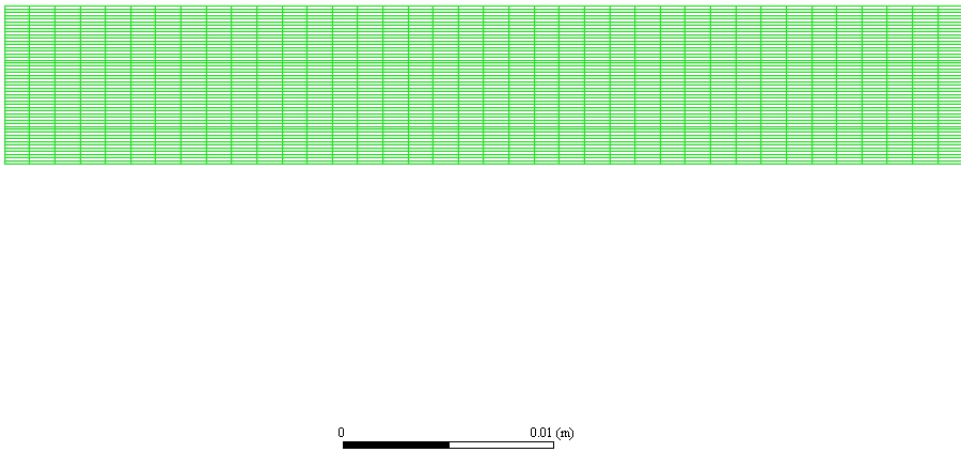

Figure 4.2: Mesh of the geometry

4.2.2. Medium

The medium contains a mixture of gas and solid. The gas mixture is composed of methane and argon which, being a noble gas, is chosen as inert carrier(instead of argon also hydrogen or nitrogen could be used as inert gas), and as the temperature raises, methane will decomposed into hydrogen an carbon inside the tube. Beside the above mention gases other gases can be produced in minor amount. These byproducts are neglected. The carbon particles surface will act as catalyst. Due to the deposition of the produced carbon the particle diameter will grow. Further the particle are considered to be spherical.

4.2.3. Gas phase absorption coefficient

In this work only methane will be taken into consideration in terms of optical attenuation behavior. It is assumed that argon and hydrogen absorbed almost no radiation. For the absorption coefficient of methane, the Planck mean absorption coefficient will be used that is given as follows:

$$\kappa_p = \frac{\int_0^\infty I_{b\lambda}\kappa_{p,\lambda}d\lambda}{\int_0^\infty I_{b\lambda}d\lambda} \tag{4.3}$$

In work of Antonio Robunio [Rubino [9]] a fourth order polynomial fit to κ_{ch4} as function of temperature is given. The expression is valid only between 300 and 2500 k.

$$\kappa_{ch4} = 6.6334 - 0.0035686T + 1.668210^{-8}T^2 + 2.561110^{-10}T^3 - 2.655810^{-14}T^4 \tag{4.4}$$

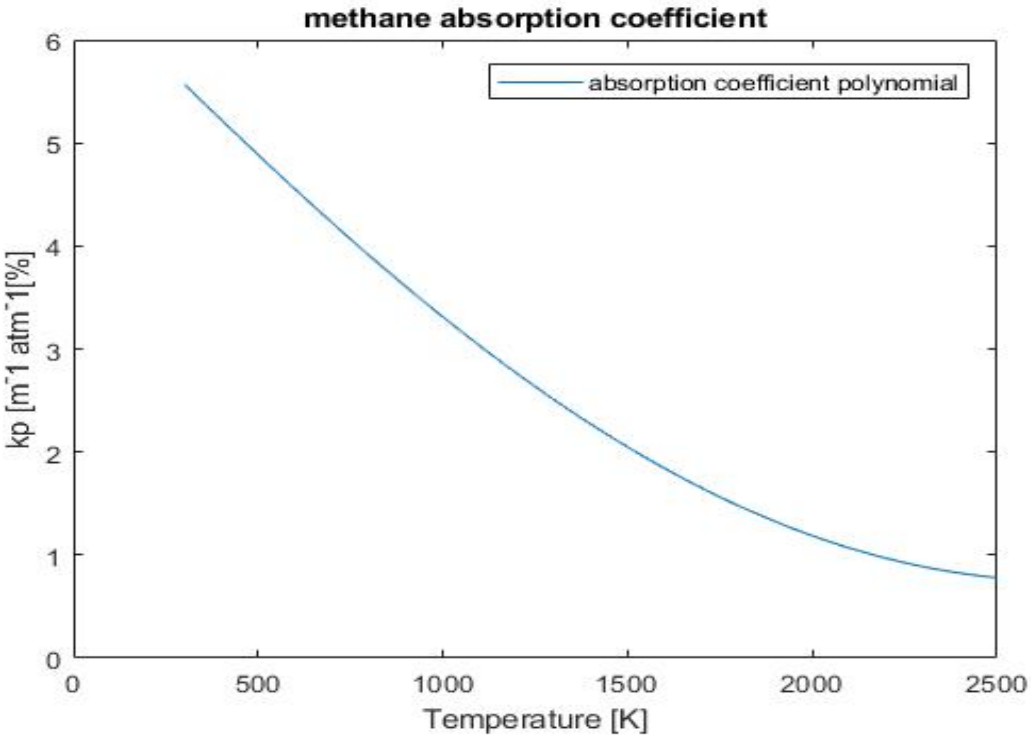

Figure 4.3: mean planck absorption coefficient

As can be seen in figure 4.3 the absorption coefficient of methane is decreasing when the temperature is increasing.

4.2.4. Carbon particle absorption coefficient

To determine the absorption coefficient of the carbon particles the Planck mean absorption and scattering efficiency are calculated by using the Mie theory. An in house build Mie theory code is used to generate the absorption efficiency ($Q_{abs,\lambda}$) and scattering efficiency ($Q_{sca,\lambda}$) and the Planck mean formula is used to get wavelength integrated values:

$$Q_{abs} = \frac{\int_0^\infty I_{b\lambda} Q_{abs,\lambda} d\lambda}{\int_0^\infty I_{b\lambda} d\lambda} \tag{4.5}$$

$$Q_{sca} = \frac{\int_0^\infty I_{b\lambda} Q_{sca,\lambda} d\lambda}{\int_0^\infty I_{b\lambda} d\lambda} \tag{4.6}$$

The Planck mean scattering and absorption efficiency data generated from the Mie code are for particle radius between 15 and 17 micrometer shown in figure 4.5 and figure 4.4. It can be seen from figure 4.4 the absorption efficiency are increasing with temperature while the scattering efficiency in figure 4.5 is decreasing with temperature but are larger than the absorption efficiency.

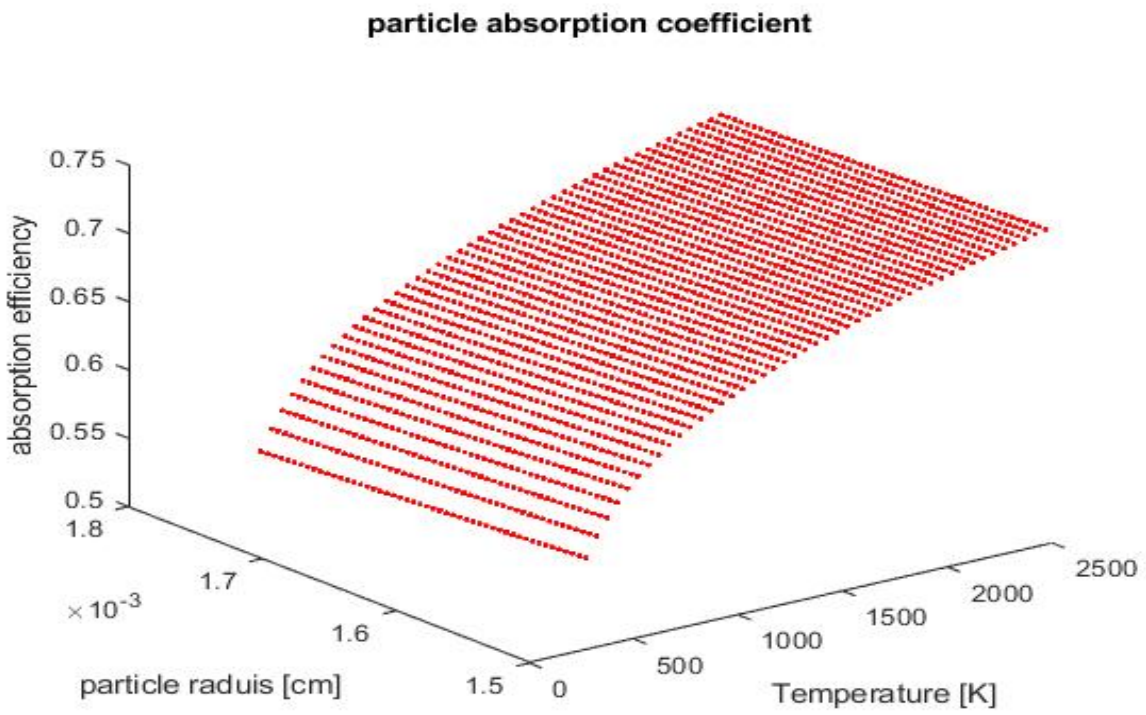

Figure 4.4: Absorption efficiency as function of diameter and temperature

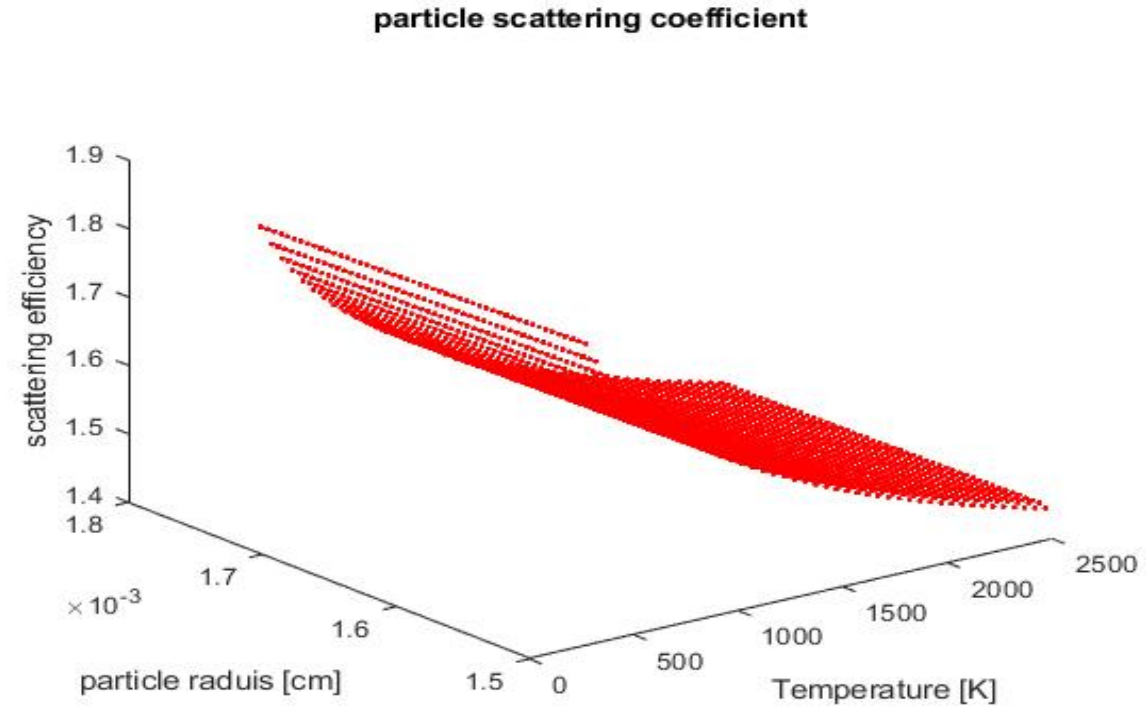

Figure 4.5: Scattering efficiency as function of diameter and temperature

A table is made for the absorption efficiency and scattering efficiency which is implemented in a user defined function. During the simulation the temperature and the diameter is read. The temperature and

diameter are interpolated by using the table data and return the absorption efficiency and scattering efficiency value to the program.

4.2.5. Discrete phase model (DPM)

Fluent allowes to simulate a discrete phase in a lagrangian frame of reference. The solid phase consist of spherical particles dispersed in the continuous phase. The discrete phase formulation in Fluent relies on the assumption that the solid phase is sufficiently dilute so that the particle-particle interaction and the effect of the particle volume fraction on the gas phase are negligible. These limitation implies that the particle volume fraction must be less than $10 - 12$ percent [Manual [23]].

In the work of Antonio Rubinio the following expression was given to calculate the particle mass flow rate at the inlet of the reactor [Manual [23]].

$$m_{p,in} = \frac{\rho_p V_{g,in} \alpha_p}{1 - \alpha_p} \tag{4.7}$$

where α_p is the particle volume faction and $V_{g,in}$ is the inlet volume flow rate in $\frac{m^3}{s}$.

The inlet parameters shown in table 4.1 were kept constant for every simulation.

X-velocity [m/s]	Y-velocity [m/s]	Diameter[m]	Temperature [k]
0.001	0	3.005e-5	300

Table 4.1: Discrate phase model: Inlet parameters for the simulation

The injection time of the particle was chosen in such a way that that simulation reach the steady state solution. The particles are injected from the inlet surface. Fluent use the concept of parcel to release the particles. This mean that the simulated cloud consists of parcels. Each parcel represents a number of identical particles. In each parcel the particles have the same properties like velocity, temperature ect.

4.2.6. Viscosity and thermal conductivity approximation

The temperature of the solar reactor increases a lot approximately from 300 K to somewhere 2500 K. This mean a large increase in the viscosity as the temperature increased. In the work of Abanades an exponential equation as function of temperature is given for the viscosity and thermal conductivity. These equation are used for the methane, hydrogen and argon [[4]]. The average viscosity and thermal conductivity is calculated by multiplying the mass fraction of each species by the exponential equation and summing that up. The viscosity and thermal conductivity is shown in figure 4.6 and figure 4.7.

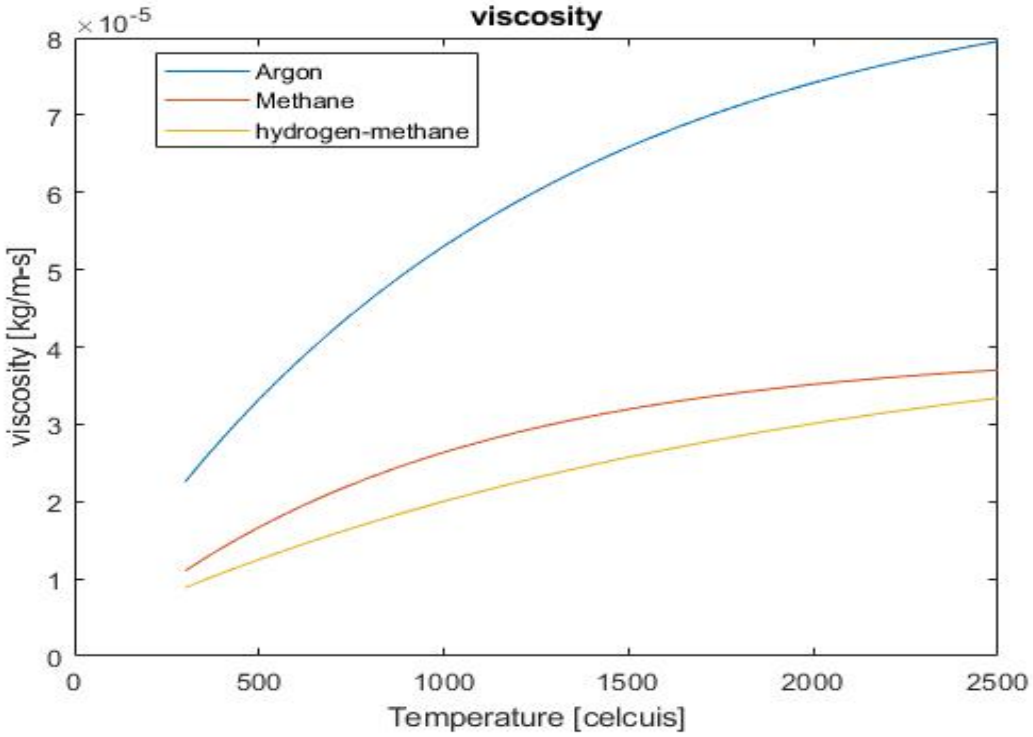

Figure 4.6: Viscosity as function of temperature

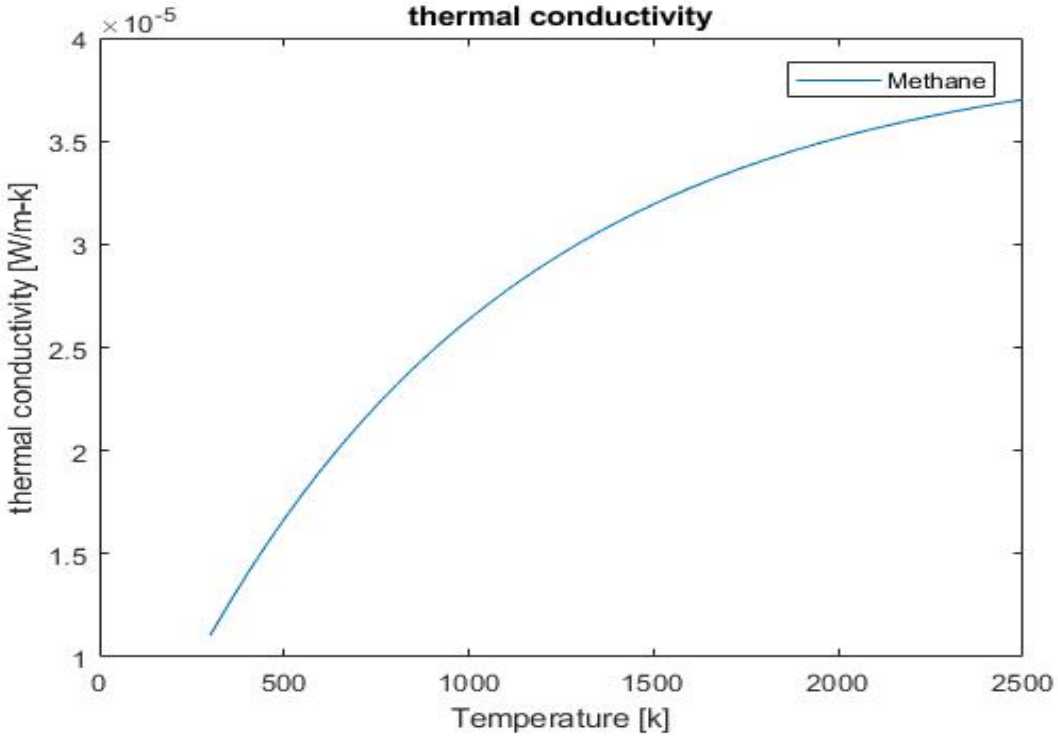

Figure 4.7: Thermal conductivity as function of temperature

In figure 4.7 only the methane thermal conductivity is given. The thermal conductivity of hydrogen is $0.18\frac{W}{mk}$ and the thermal conductivity of argon is $1.77 \times 10^{-2}\frac{W}{mk}$.

4.2.7. Mass Diffusivity constant

The binary mass diffusivity as function of pressure and temperature is calculated by using Hirschfelder equation.

$$D_{AB,T2,P2} = D_{AB,T1,P1}\left(\frac{P1}{P2}\right)\left(\frac{T2}{T1}\right)^{\frac{3}{2}}\frac{\Omega_{T1}}{\Omega_{T2}} \tag{4.8}$$

Where $D_{AB,T2,P2}$ is the mass diffusivity of specie A and species B. Ω is the collision integral. In figure 4.8 the mass diffusivity is plot of argon-methane, argon-hydrogen and methane-hydrogen. In our application the pressure remain constant $p_1 = p2$.

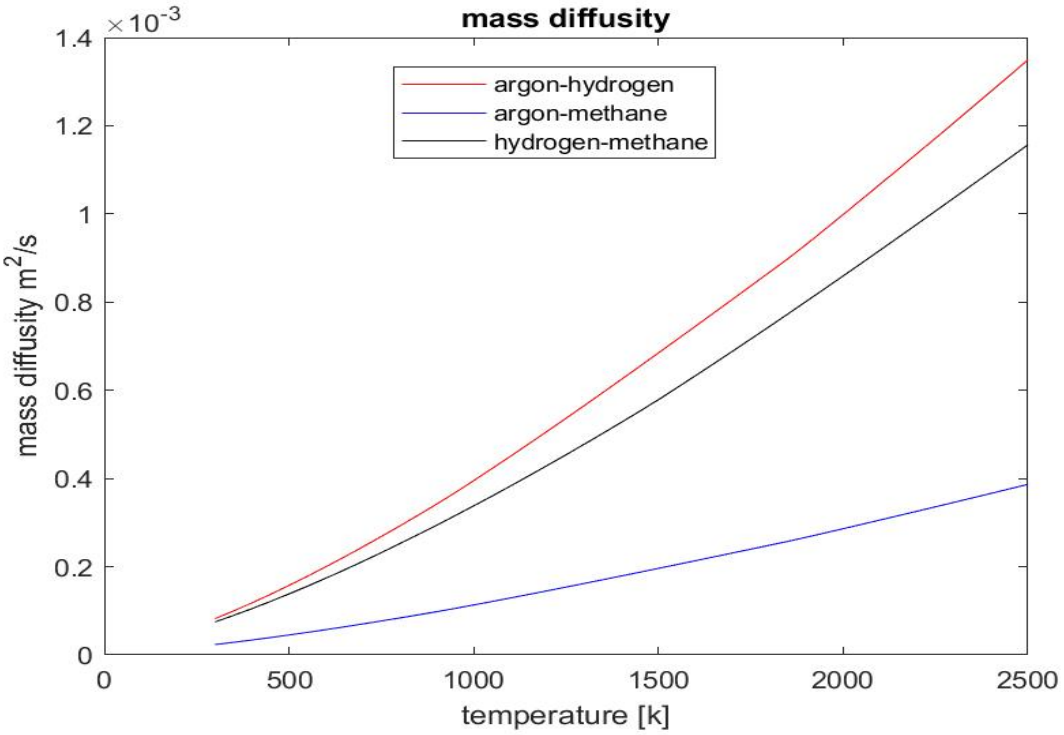

Figure 4.8: Mass diffusivity as function of temperature

4.2.8. Schemes for the continuous phase

The following numerical discretization schemes in table 4.2 and under relaxation factors in table 4.3 have been adopted for the solution of the transport equations.

Equation	Discretization
Pressure	Standard
Momentum	second order upwind
Y_{ch4}	second order upwind
Y_{h2}	second order upwind
Energy	second order upwind
Discrete ordinates (radiation)	second order upwind
Pressure-Velocity	Simple

Table 4.2: Numerical Discretization schemes.

Equation	Under relaxation factors
Pressure	0.3
Momentum	0.8
Y_{ch4}	0.8
Y_{h2}	0.7
Energy	0.8
Discrete ordinates	0.9

Table 4.3: Under relaxation factors

5

Results

In this chapter numerical simulations of steady state operation of the tabular reactor are performed. The goal of the numerical simulation is to see how different parameters influence the methane and hydrogen conversion. During the numerical simulation the influence of the particle mass fraction, wall heat flux and methane inlet molar fraction were studied. To calculate the methane and hydrogen yield equation 3.43 and equation 3.44 from chapter 3 are used.

5.1. Validation of the model

In the work of Cyril Caliot[Caliot *et al.* [7]] a numerical simulation was performed on the same tubular reactor using a different set of models. To give a general indication what Caliot did and what is done in this work the models are listed in table 5.1.

Topic	Caliot	This work
reactor	2D model	2D model
Flow dynamics	Navier-Stokes	Navier-Stokes
Heat transport	energy equation	energy eguation
radiation tranport	discrete ordinate radiation model	discrete ordinate radiation model
Species transport	advection-diffusion-reaction	advection-diffusion-reaction
carbon particle	spherical	spherical
particle distribution	sectional method	Each particle own size
particle processes	nucleation, heterogeneous reaction, coagulation	heterogeneous reaction
reaction mechanism	single step	single step
particle volume fraction	10^{-5}	$10^{-4}, 10^{-5}$
Gas phase species	methane, hydrogen and argon	methane, hydrogen and argon
radiation spectral model	Absorption distribution function and Mie theory	Mean Plack absorption coefficient and Mie theory to generate a table for calculating the particle absorption and scattering coefficient.
Boundary condition	The reactor wall is separate into two zones, first 200 mm temperature is linearly increasing from 300 to 1800 K and after that the temperature is fix at 1800 K	At the wall the a heat flux is set

Table 5.1: Overview of models used in Caliot's work and the present work[Caliot *et al.* [7]]

In table 5.1 an overview is given of the model that is used in Caliot's work. As can be seen in table 5.1 Caliot's work contains nucleation and coagulation models and in this work these two are neglected. For the methane absorption coefficient the absorption distribution function is used and in this work the Planck mean absorption coefficient is used. Caliot divided the particle size in different classes which is known as sectional method and in each section is calculated and in this work the amount of mass the particle growth is calculated for each particle. The temperature on the wall is set as described in table5.1 and in this work a wall heat flux is set at the wall of the reactor. The work of Caliot indicates that inside the reactor a boundary layer was developed, which result in significant variation of the local particle size distribution across the reactor. The same can be said in present work. Near the wall the temperature is higher than in the center of the tube. At high temperatures the methane reaction happens which leads to the diameter to grow faster near the tube wall and slower near the center of the reactor. Due to this the diameter variation across the tube is simular to the diameter variation found in the work of Caliot. The three zones identified in the work of Caliot are the pre heating zone, the reaction zone and the post reaction zone. In the pre heating zone, the fluid and the particle are heated, in the reaction zone the methane reacts on the surface of the particles and in the post reaction zone the particle, the reaction product and the not reacted methane remain present. All these three zone can be identified in this work. In this way we can qualitatively verify the model with the work of Caliot *et al.* [7].

5.2. Evolution of Dimensionless numbers

The dimensionless form of the transport equations was derived. When the transport equation was made dimensionless the following dimensionless numbers: Reynolds number, Schmidt number, Prandtl number, Planck number and Damkohler. The dimensionless numbers depends on the reference values that are chosen. The values of these reference values depend on the position in the reactor and therefore also the dimensionless numbers can change. The dimensionless number is calculated only for one case. The initial condition are for case 1 which is shown in table 5.3.

First the Reynolds number is plot along the axis of the tube.

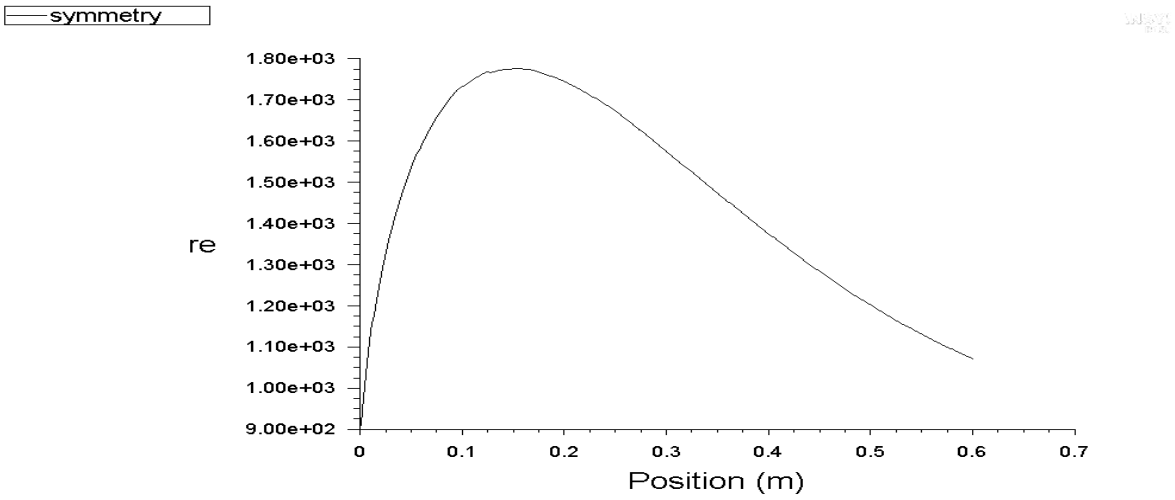

Figure 5.1: Reynolds number as function of axial position in the tube.

As can be seen the Reynolds number is plot near the center of the tube. The Reynolds number is define as $\frac{\rho UD}{\mu}$. The density(ρ), velosity (U), viscosity (μ) is depending on the position of the flow and the D is the tube diameter. The maximum Reynolds number is lower that 2300 which mean the flow is laminar. In figure 5.2 and figure 5.3 the density and viscosity at axis along the axial direction is given.

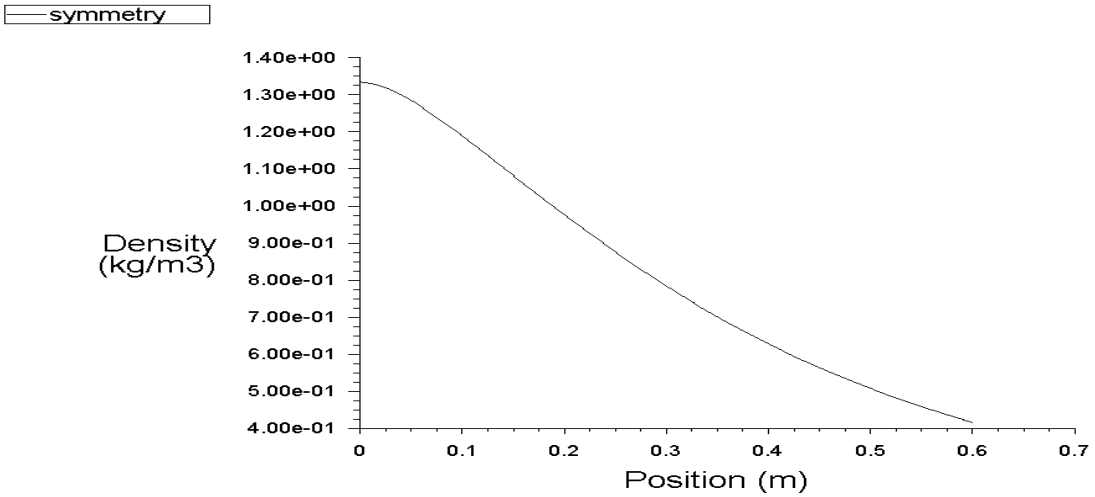

Figure 5.2: The fluid density as function of axial position on the axis.

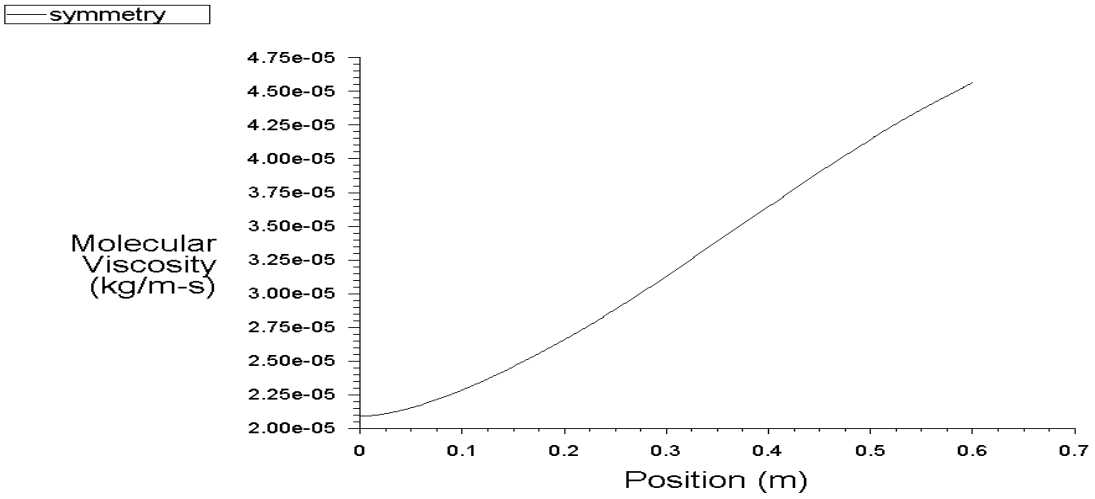

Figure 5.3: The fluid viscosity on the axis as function of axial position.

In the figure 5.2 can be seen that the density of the fluid is decreasing along the axis in the axial direction. The temperature is increasing due to this the fluid expended and the density decrease. In the figure 5.3 the viscosity plot is shown at the axis of the tube in the axial direction. The viscosity of the fluid is temperature dependent and increase along the axial direction as shown in the figure. Because the viscosity, density and the velocity of the fluid is position dependent of the flow the Reynolds number is also position dependent of the flow which is shown in figure 5.1.

Second the Prandtl number is plotted near the wall of the tube in the x direction.

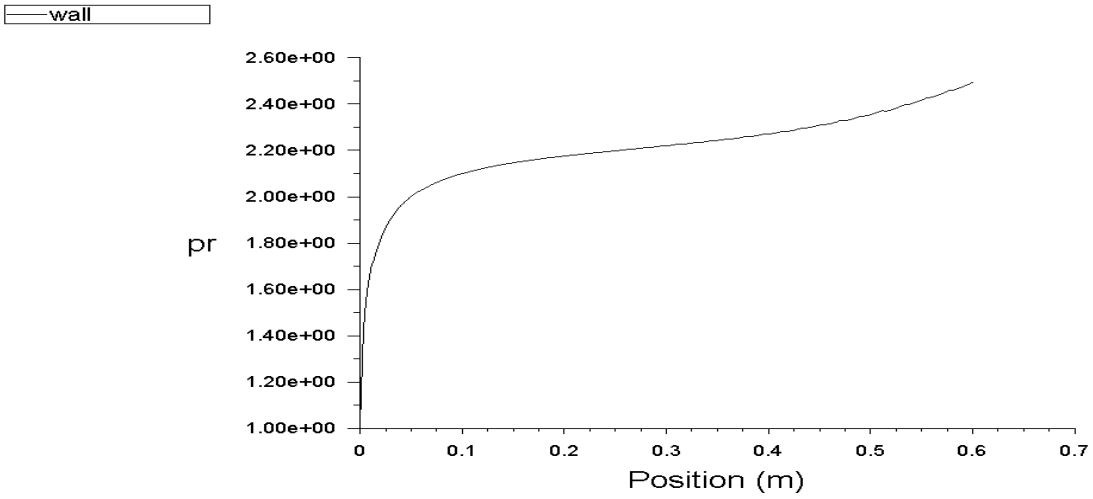

Figure 5.4: Prandtl number near the wall as function of the axial position.

The Prandtl number is define as follow $\frac{c_{p,o}\mu_o}{\lambda_o}$. The density, viscosity and the specific heat($c_{p,o}$) is depending on the position of the flow and is changing continuously as shown in figure 5.4. From the figure 5.4 the Prandtl number is increasing in the x direction along the wall. From the figure 5.4 can be observed that the momentum diffusion become more important than the thermal diffusion. The density, viscosity and the specific heat is plot near the wall in the axial direction which is shown below.

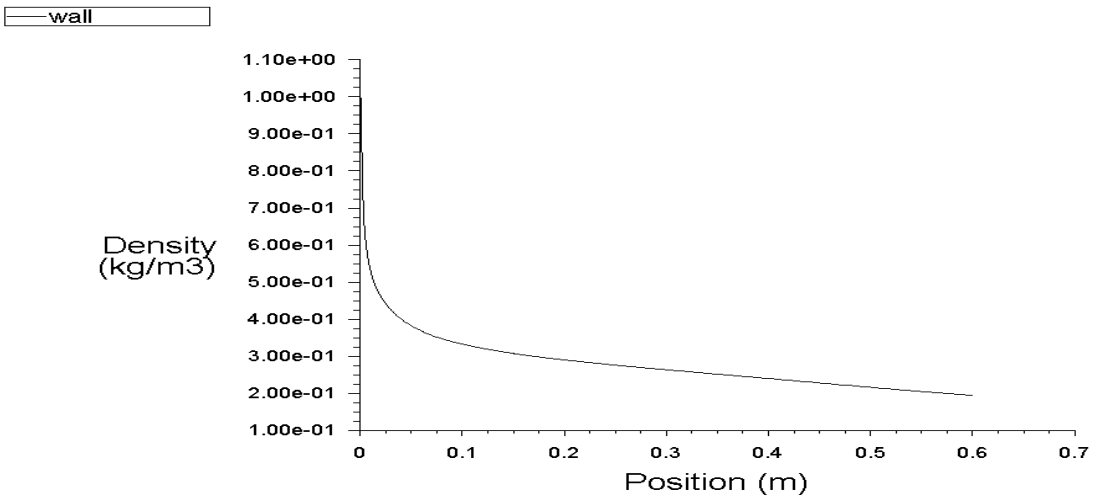

Figure 5.5: fluid density near the wall as function of axial position in the tube.

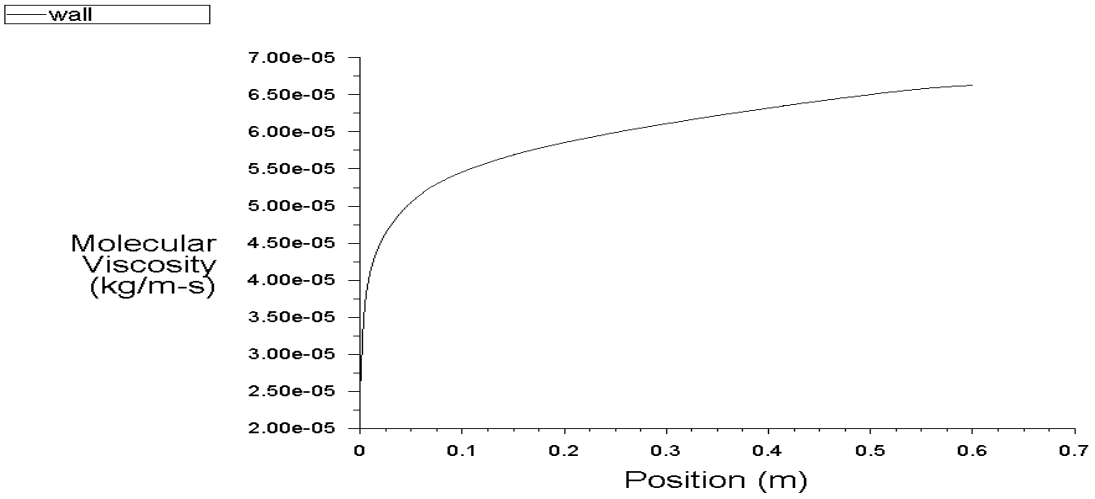

Figure 5.6: Molecular viscosity as function of the axial position in the tube.

As can be seen from figure 5.5 the density is decreasing near the wall in the axial direction and the viscosity in figure 5.6 is increasing near the wall in the axial direction.

Third the Schmidt number is plotted near the wall of the tube.

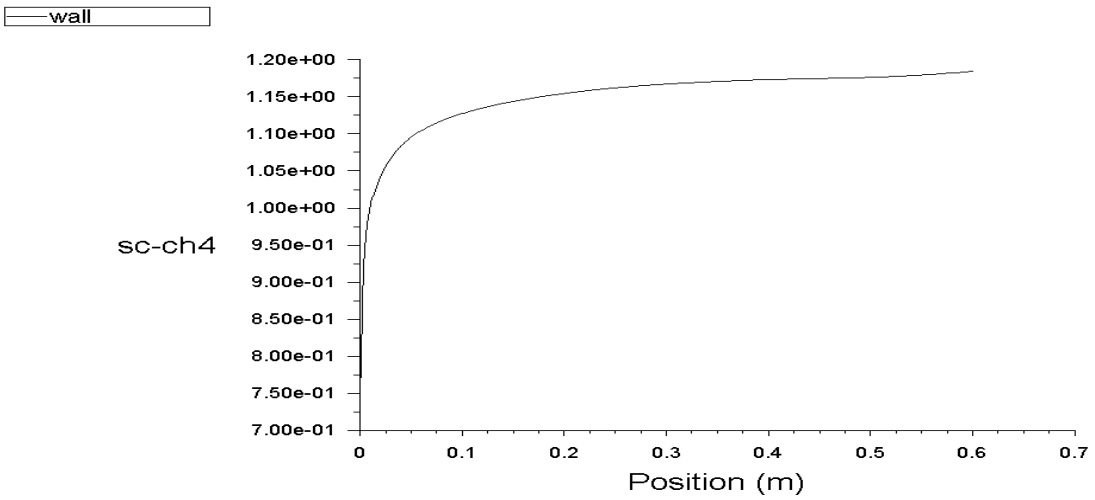

Figure 5.7: Schmidt number base on methane diffusivity constant near the wall as function of the axial position in the tube.

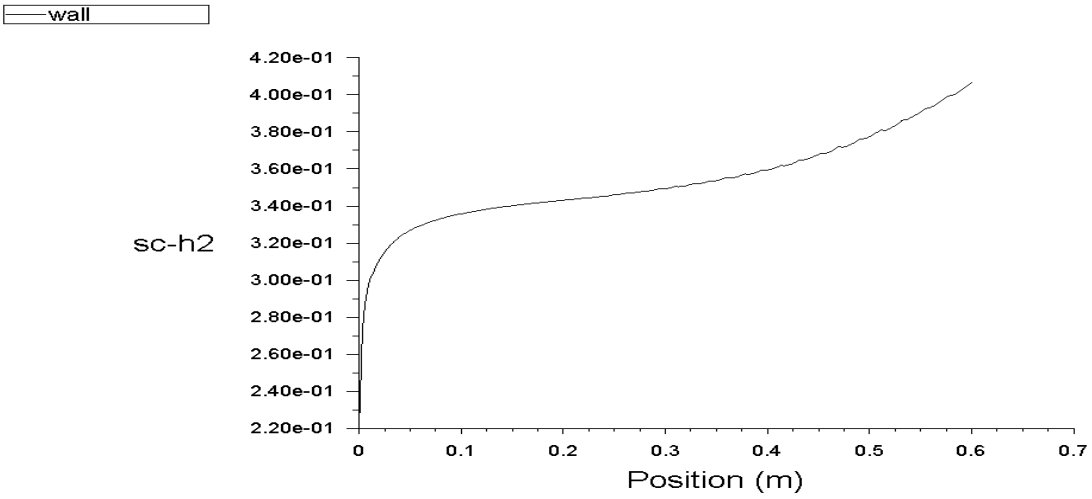

Figure 5.8: Schmidt number base on hydrogen diffusivity constant near the wall as function of the axial position in the tube.

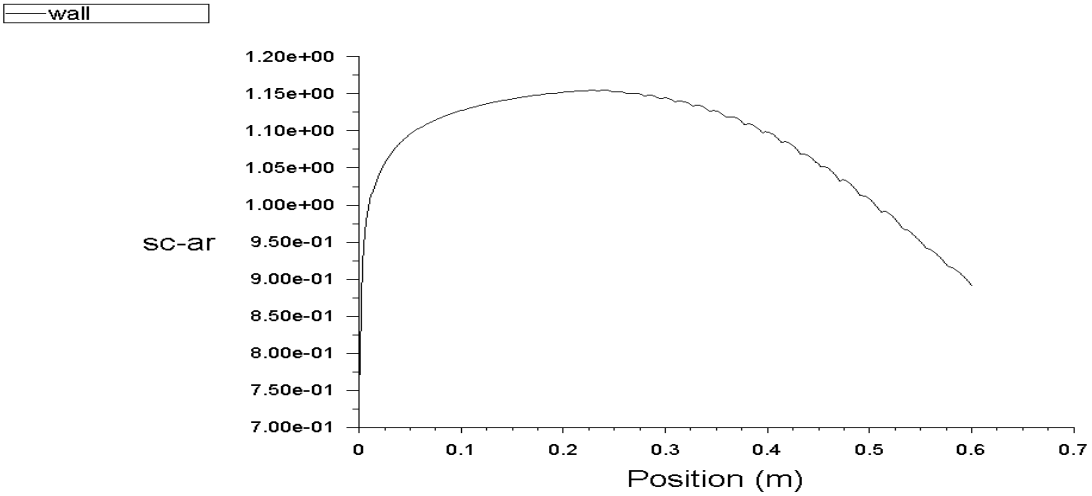

Figure 5.9: Schmidt number based on methane diffusivity constant near the wall as function of the axial position in the tube.

The Schmidt number is defined as follow $\frac{\nu}{D_{k,g,o}}$. Kinematic viscosity (ν) and mass diffusivity constant are depending on the position of the flow. Further the Schmidt number can be based on the mass diffusivity of methane, argon or hydrogen. The results are shown in the above figures. The Schmidt number based on methane mass diffusivity is increasing from the inlet and follows a horizontal line in the x direction. This means that both the momentum diffusivity and mass diffusivity are important. Schmidt number based on hydrogen is increasing near the wall in the x direction and based on argon it is first increasing and than decreasing along the wall. The mass diffusivity constants of argon, hydrogen and methane are temperature dependent and depend on the position of the flow. The mass diffusivity of argon, hydrogen and methane near the wall in the axial direction is given in the figures below.

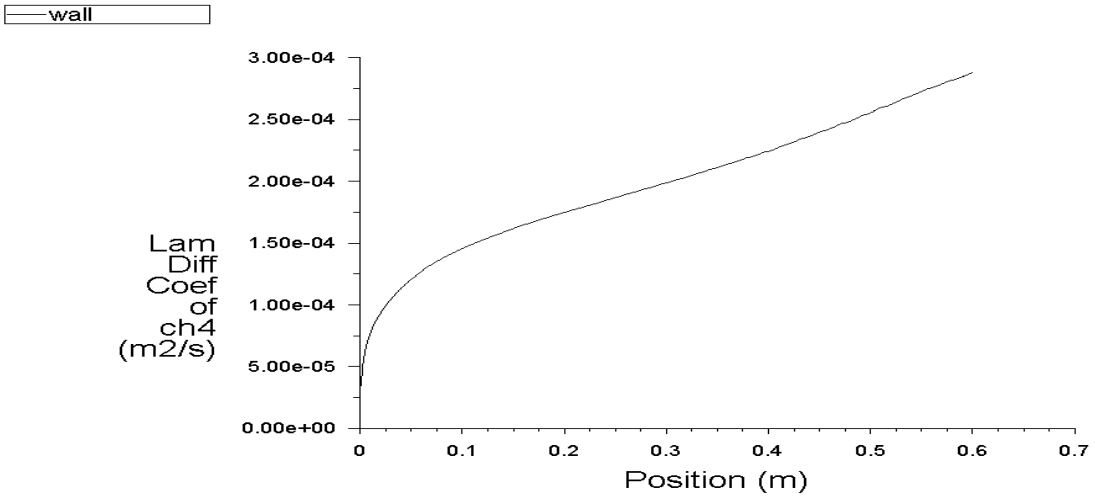

Figure 5.10: Mass diffusivity of methane gas near the wall as function of axial position in the tube.

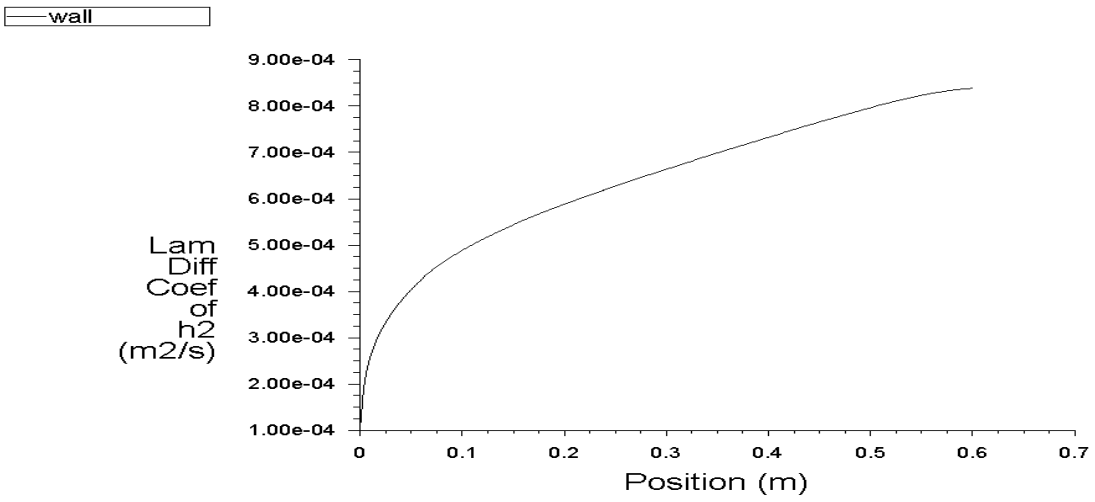

Figure 5.11: Mass diffusivity of hydrogen gas near the wall as function of axial position in the reactor.

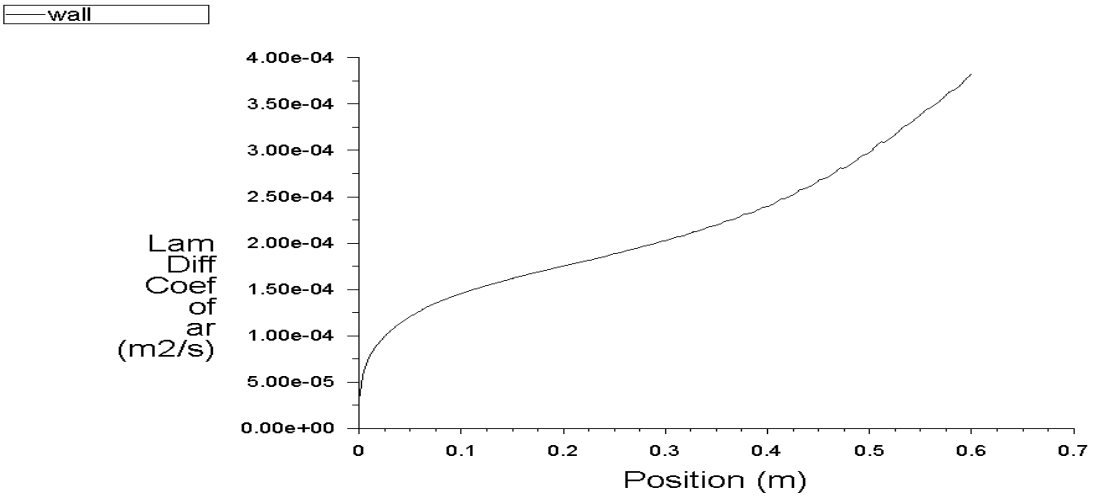

Figure 5.12: Mass diffusivity of argon gas near the wall as function of axial position in the reactor.

Fourth the Planck number can defined in two way as shown in table 3.1. In figure 5.13 the Planck number is plot by using the formula of Planck 1 and in figure 5.14 by using the formula of Planck 2.

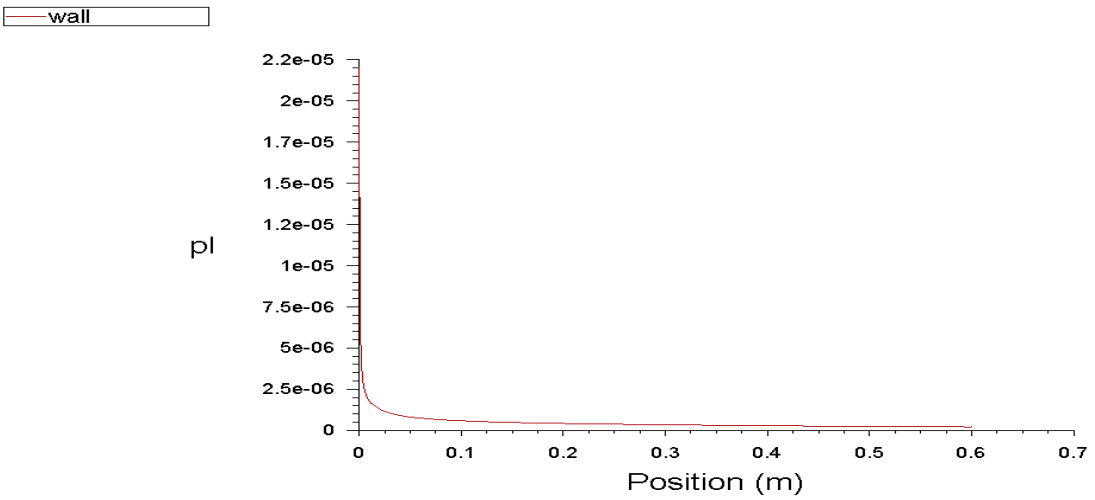

Figure 5.13: Planck number near the wall as function of axial position in the reactor.[Planck 1]

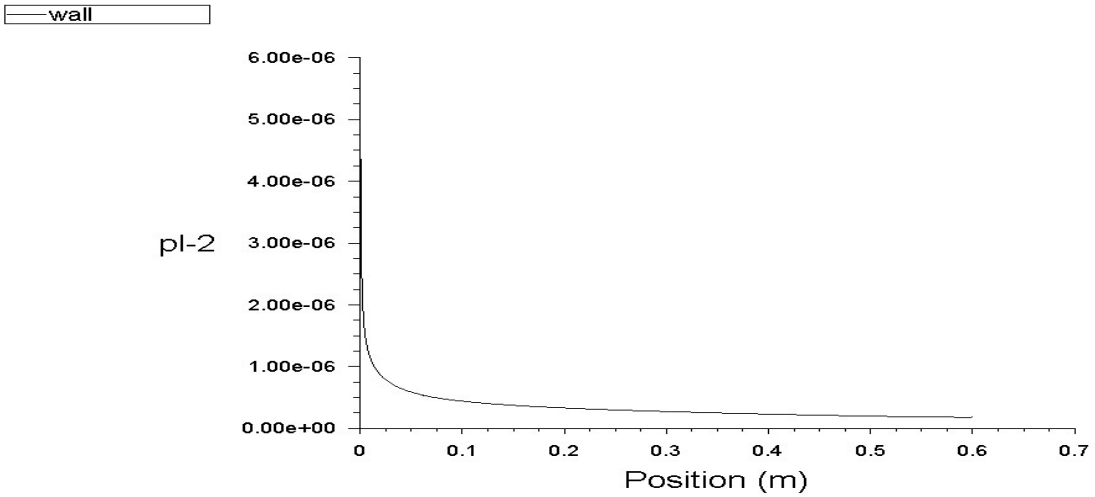

Figure 5.14: Planck number near the wall as function of axial position in the reactor with $T_{ref} = 300K$.[Planck 2]

As can be seen in figure 5.13 the Planck number is decreasing from 2.2×10^{-5} to zero. Which means that the radiative heat transfer is dominant. In figure 5.13 we see that radiation is dominant in the system but the fluid is not further heating up . This is because heat is also extracted from the surface of the particle for the reaction of methane. Due to this less heat is transfer by conduction into the fluid. In figure 5.14 the Planck number is plotted by using the formula of Planck 2. The same conclusion can be said as using the formula of planck 1. It is seen from the low Planck number radiation heat transfer is very important than conductive heat transfer. But the amount of radiation that is absorbed by the particles also depend on the absorption coefficient. So in this case the radiation heat transfer is dominant only when the absorption coefficient is high.

The last one is the Damkohler number which is plotted below:

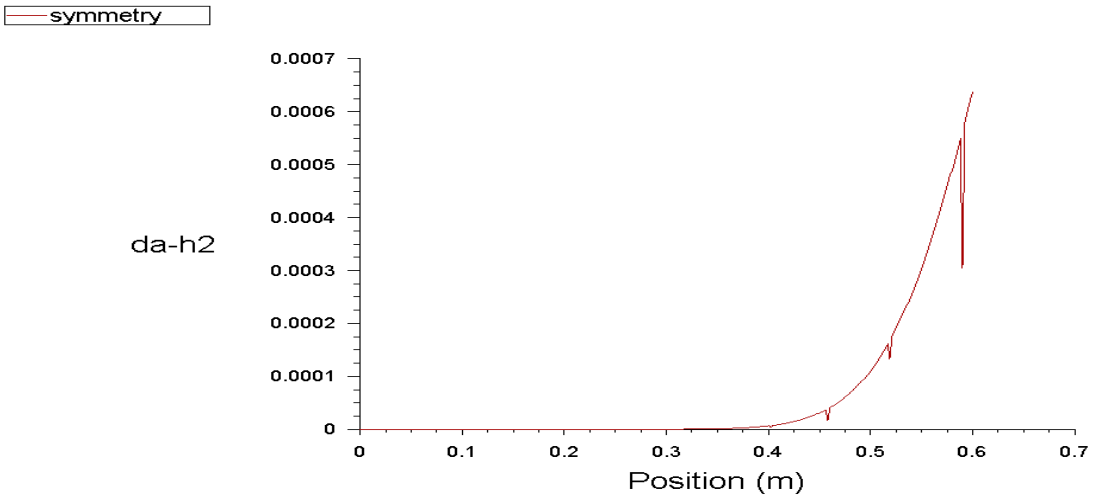

Figure 5.15: Damkohler number base on hydrogen diffusivity constant near the wall as function of axial position in the tube.

The Damkohler number is define as $\frac{R_o D}{\rho_o U_o y_o}$. The reaction rate ($R_o$) of hydrogen is calculated in the user

defined function at each position of the flow. The hydrogen mass fraction (y_o), velocity and density are depending on the position of the flow. As can be seen in the figure 5.15 the Damkohler number is low which mean that the convective transport is faster than the chemical reaction . The low Damkohler number explains why the methane conversion into hydrogen and carbon is low.
To give a quantitative information on how the dimensionless number are changing in the axial direction the values of the dimensionless number are given in table 5.2 at axial position of $300mm$ and $600mm$. The y positions for each number are the same as the figures above.

Dimensionless number	at x=300 mm	x=600 mm
Re	1600	1100
Pr	2.2	2.5
Sc-ch4	1.15	1.17
Sc-h2	0.35	0.4
Sc-ar	0.9	1.15
Da	0	6×10^{-4}
Pl 1	5×10^{-7}	5×10^{-7}
Pl 2	1.2×10^{-7}	2.5×10^{-7}

Table 5.2: Overview of the dimensionless number at axial position of 300 mm and 600 mm

5.3. Influence of particle volume fraction

To check the influence of the particle volume fraction of hydrogen production and the methane conversion the particle volume fraction was taken either of 10^{-4} or 10^{-5}. The boundary condition is shown in table 5.3

Case number	Initial particle diameter size [μm]	Initial particle velocity [$\frac{m}{s}$]	Particle inlet volume fraction [–]	Methane inlet molar fraction [–]	wall heat flux [kW]	length of tube [mm]
Case 1	30	10^{-3}	10^{-4}	0.297	10	600
Case 2	30	10^{-3}	10^{-5}	0.297	10	600

Table 5.3: Boundary condition for case 1 and 2

Below the temperature, velocity, methane molar fraction, hydrogen molar fraction, the particle temperature, the particle velocity, Particle mass fraction and the particle diameter contour plot is shown for case 1 and 2. In all figures the computational domain is shown with inflow from the left, outflow from the right, wall at the upper side and symmetry axis at the lower side of the figure. The real distance is scaled with a factor of 10 compared the axial distance.

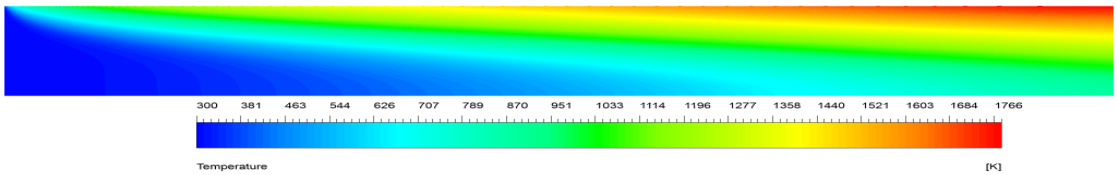

Figure 5.16: Temperature contour plot of case 1.[$\alpha_p = 10^{-4}$]

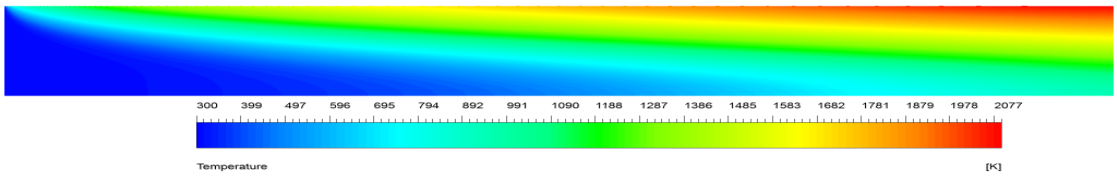

Figure 5.17: Temperature contour plot of case 2.[$\alpha_p = 10^{-5}$]

The Temperature plot of case 1 and case 2 is shown in figure 5.16 and in figure 5.17. As can be seen from the figures that the wall temperature increased from left to right. As the fluid is flowing from the inlet to outlet the temperature of the fluid is increasing. In both cases a temperature boundary layer is developed and the thickness of the boundary layer is increasing in the direction of the outlet. In case 1 the maximum temperature in the tube is 1766 K and in case 2 it is 2077 K. In case 2 the maximum temperature is higher than in case 1. A explanation for the lower maximum temperature is as follow: In case 1 the methane conversion is higher than in case 2. The net heat of reaction is extracted from the surface of the particles. Due to this more heat is extracted from the surface of the particle in case 1 than in case 2. Due to this less heat is transfer by conduction to the fluid. Because of this the maximum fluid temperature is lower than in case 2.

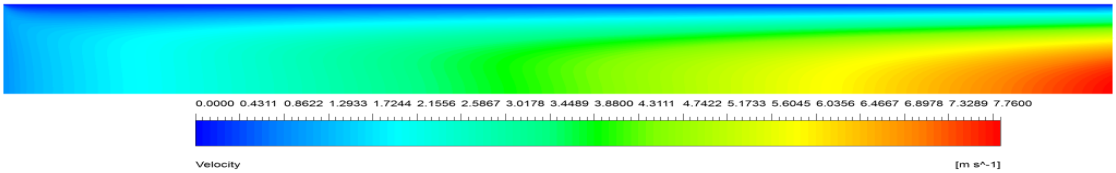

Figure 5.18: Velocity contour plot of case 1.[$\alpha_p = 10^{-4}$]

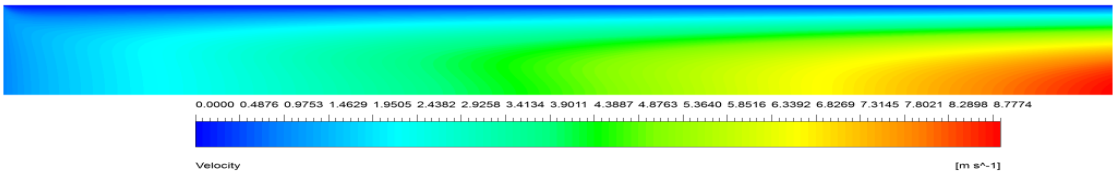

Figure 5.19: Velocity contour plot of case 2.[$\alpha_p = 10^{-5}$]

The fluid starts flowing from the inlet with a velocity of $0.95\frac{m}{s}$ in the axial direction and developing a velocity profile with maximum velocity near the center of the tube and zeros near the wall of the tube because of no slip boundary condition. The maximum velocity in case 1 is $7.76\frac{m}{s}$ and in case 2 is $8.77\frac{m}{s}$. The maximum velocity is higher in case 2 than in case 1. This is because of the higher temperature in case 2 the fluid expands more and due to this the velocity increases more than in case 1.

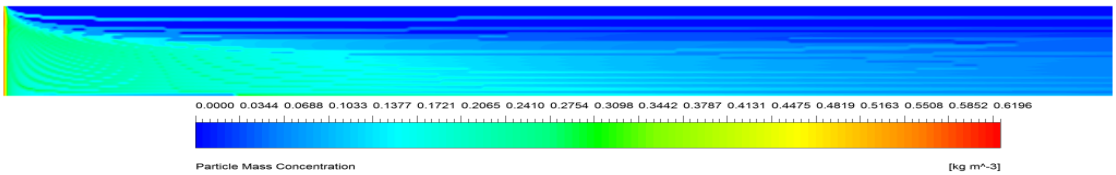

Figure 5.20: Particle mass concentration contour plot of case 1.[$\alpha_p = 10^{-4}$]

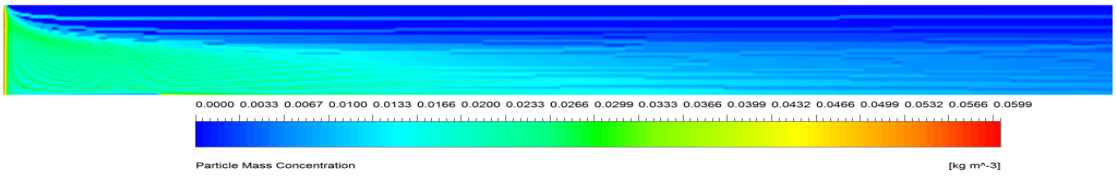

Figure 5.21: Particle mass concentration contour plot of case 2.[$\alpha_p = 10^{-5}$]

The particle mass concentration of case 1 and case 2 is shown in figure 5.20 and in figure 5.21. The particle is injected from the inlet of the tube which mean that at the inlet the particle mass concentration must be uniform as shown in the figures. As shown in figure 5.20 and in figure 5.21 the particle mass concentration decreases in the axial direction. This is because of the temperature is increases and due to this the density of the fluid is decreases. Second due to the reaction the seed particles diameter is increasing.

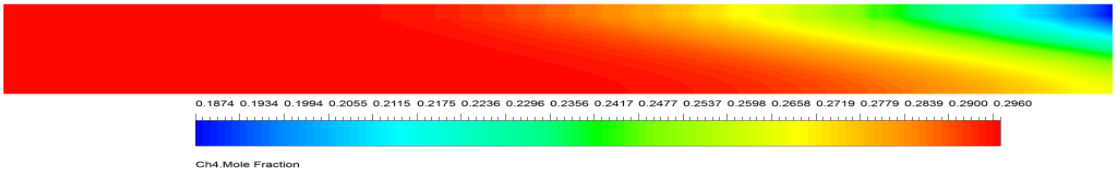

Figure 5.22: Methane molar fraction contour plot of case 1.[$\alpha_p = 10^{-4}$]

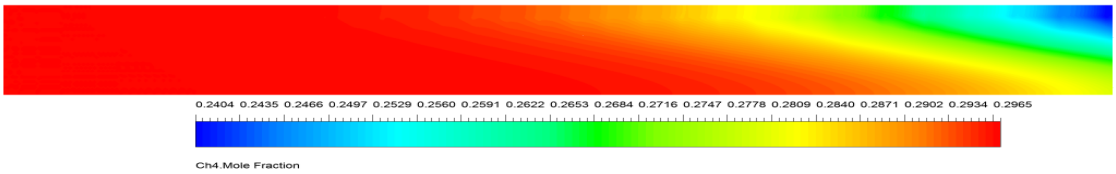

Figure 5.23: Methane molar fraction contour plot of case 2.[$\alpha_p = 10^{-5}$]

The methane molar fraction plot of case 1 and case 2 is shown in figure 5.22 and in figure 5.23. The reaction rate is temperature dependent: at higher temperature more methane will be converted into hydrogen and carbon particles. The conversion of methane takes place on the surface of the particles. In case 2 the particle volume fraction is lower than in case 1 which results in lower methane conversion as can be seen in figure 5.23. Although the temperature is higher in case 2, less particle surface is available for the reaction of methane. So from the above the following can be concluded that to increase the methane conversion the temperature and the particle mass should be increased.

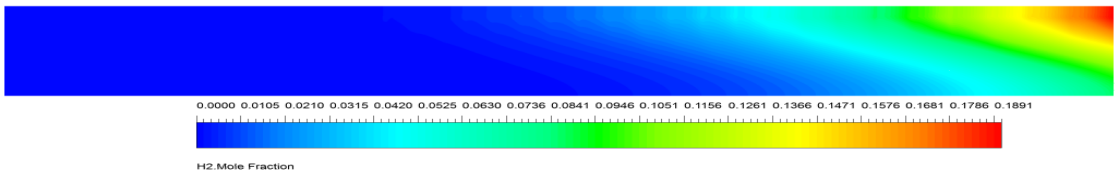

Figure 5.24: Hydrogen molar fraction contour plot of case 1.[$\alpha_p = 10^{-4}$]

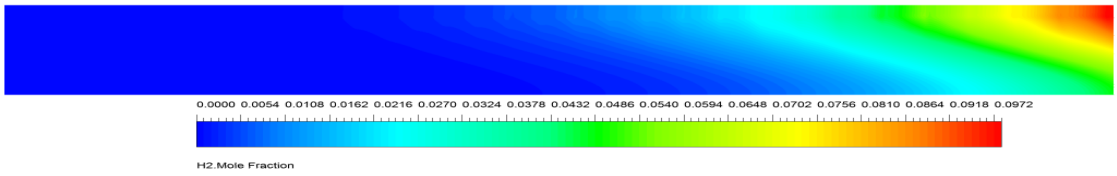

Figure 5.25: Hydrogen molar fraction contour plot of case 2.[$\alpha_p = 10^{-5}$]

The hydrogen molar fraction of case 1 and case 2 is shown in figure 5.24 and in figure 5.25. As was discussed for the methane molar fraction also the hydrogen molar fraction is higher in case 1 than in case 2 because of more particle surface is available for the reaction.

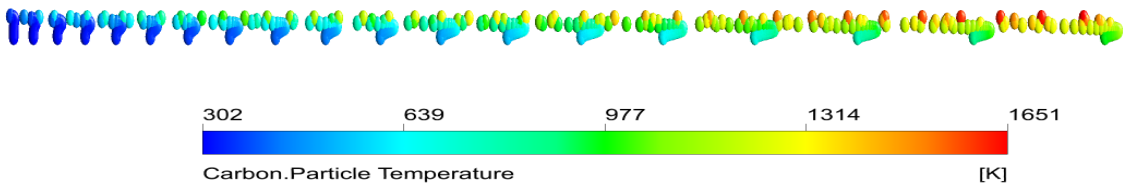

Figure 5.26: Particle colored by Temperature of particle in case 1.[$\alpha_p = 10^{-4}$]

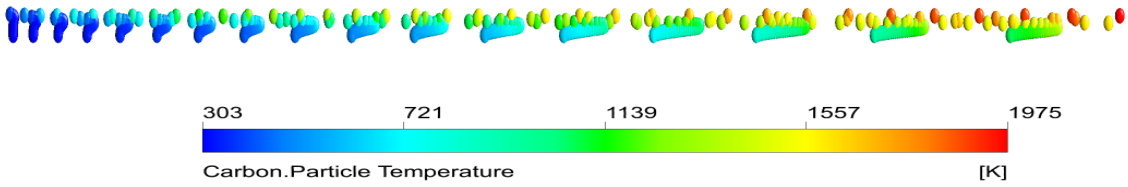

Figure 5.27: Particle colored by the temperature of particle in case 2.[$\alpha_p = 10^{-5}$]

The particles are entering via the inlet and flow toward the outlet. The particles are heated by radiation and heat is transfered from the surface of the particles to the gas by conduction. From the figure 5.26 the maximum particle temperature for case 1 is $1651K$ and from figure 5.27 for case 2 is $1975K$. It can be seen from the temperature plot that the maximum gas temperature is slidely higher than the maximum particle temperature. This could be because the particle heats the fluid first by conduction but after a while the fluid is also heated by wall through conduction. An other reason is due to the reaction on the surface of the particle the particle temperature is decreases.

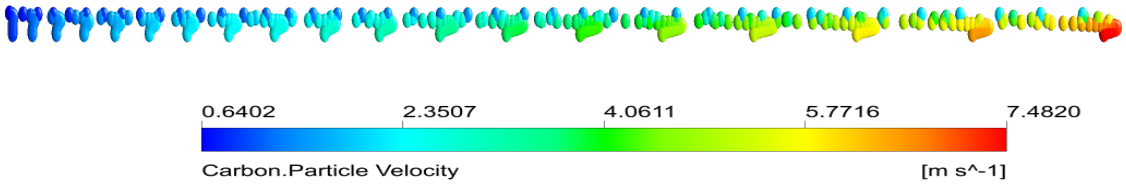

Figure 5.28: Particle colored by the velocity of particle for case 1.[$\alpha_p = 10^{-4}$]

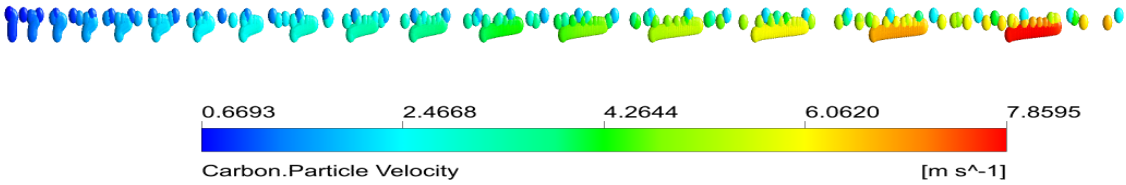

Figure 5.29: Particle colored by the velocity of particle for case 2.[$\alpha_p = 10^{-5}$]

The particle velocity plot for case 1 and case 2 is shown in figure 5.28 and in figure 5.29. The particles are released with a inlet velocity of $10^{-3}\frac{m}{s}$ and reach a maximum velocity for case 1 $7.48\frac{m}{s}$ and for case 2 $7.86\frac{m}{s}$ which is slightly lower that the maximum fluid velocity in both cases. It can be concluded that the particles adjust to the fluid velocity. To prove the expectation that the particle will follow the fluid velocity the stokes number is plotted in figure 5.30 for case 1. The stokes number is define as follows: $\frac{\rho_p d_p^2 U}{18 \nu_g D}$. In figure 5.30 the maximum stoke number is 1.15 which implies that the particle will follow the fluid velocity.

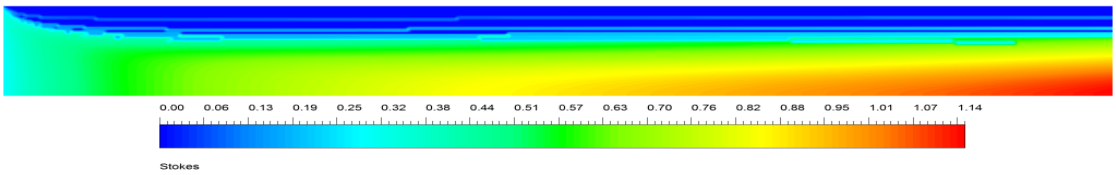

Figure 5.30: Stokes number contour plot for case 1.[$\alpha_p = 10^{-4}$]

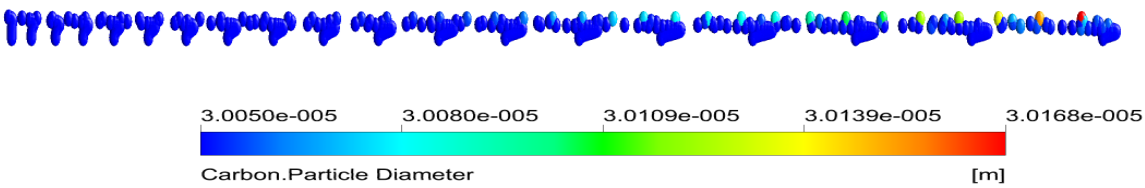

Figure 5.31: Particle colored by particle diameter for case 1.[$\alpha_p = 10^{-4}$]

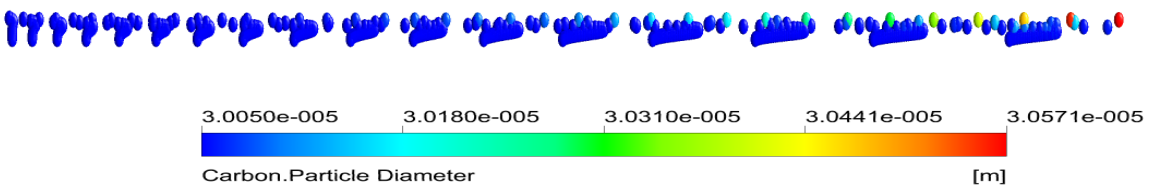

Figure 5.32: Particle colored by particle diameter for case 2.[$\alpha_p = 10^{-5}$]

The particle diameter changes due to the production of carbon. The produce carbon sticks to the seed carbon particle which leads to diameter growth. Because the temperature is higher near the wall of the tube as the fluid is flowing from the inlet to the outlet, the same is valid for the particle as shown in particle temperature plot. Carbon is produced near the wall where the temperature is higher and their the carbon sticks to the seed carbon and the diameter changed. In the figure 5.31 the maximum particle diameter is 3.0168 micrometer for case 1 and for case 2 in figure 5.32 is read 3.057 micrometer. The maximum particle growth in case 2 is larger than in case 1. This could be due to less particle is present in case 2 which mean that less surface is available for sticking the produced carbon. As seen in the particle temperature plot the temperature of the particle in case 2 is higher than in case 1. Due to this more carbon is produce which will finally stick to the seed particle and lead to diameter growth.

The methane and hydrogen molar fraction at the outlet of the tube are plotted in figure 5.33 as function of the radial distance y.

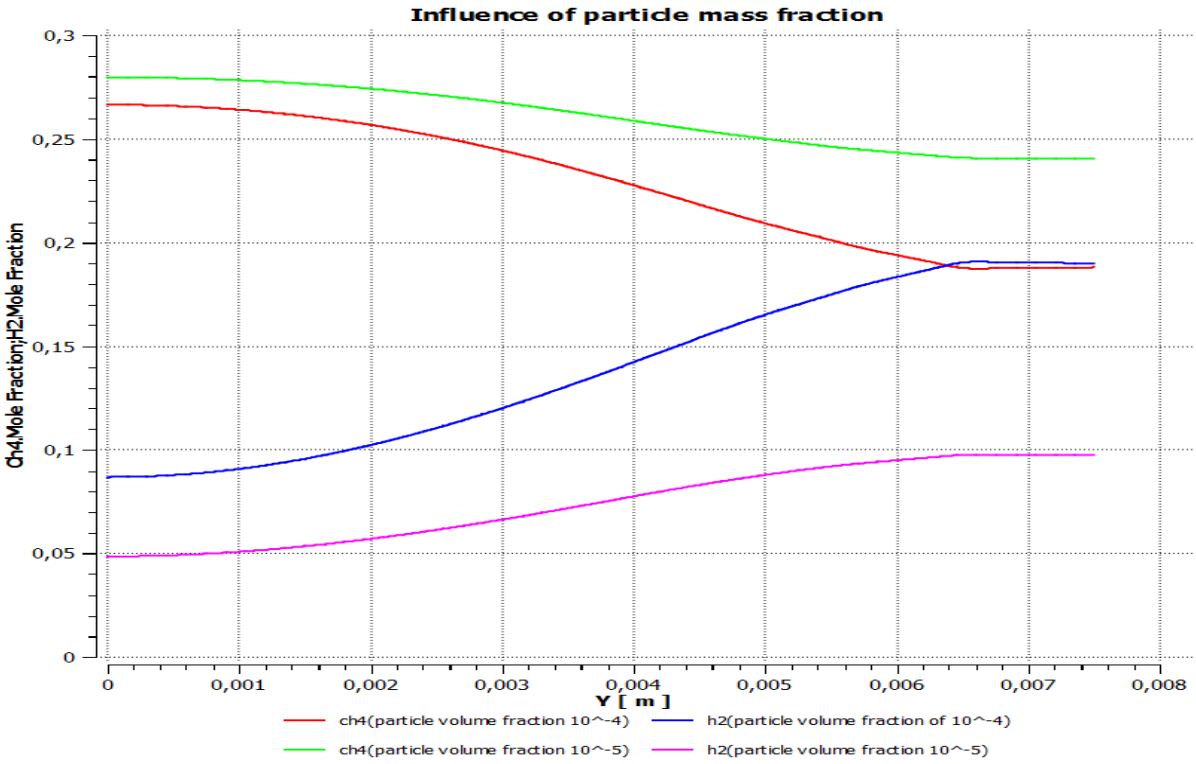

Figure 5.33: Methane and hydrogen molar fraction at the outlet of the tube in the radius direction for particle mass fraction of 10^{-4} and 10^{-5}.

As can be seen in figure 5.33 in case of higher particle mass fraction less methane molar fraction and more hydrogen molar fraction is present at the outlet of the tube than for lower particle mass fraction. Because of more particles present in the domain there is more surface reaction and more methane is converted into hydrogen. The methane and hydrogen conversion at the end of the tube in case 1 is 22.69 % and 23.28 %. For case 2 the methane and hydrogen conversion is 12.19 % and 12.48 %.

5.4. Influence of the reactor length

To see the influence of the reactor length on the methane and hydrogen conversion the length has been extended from $600mm$ to $1000mm$. All other parameters were kept constant as shown for case 1 in table 5.3. The methane and hydrogen molar fraction profiles at the outlet of the tube in the radial direction is shown in figure 5.34.

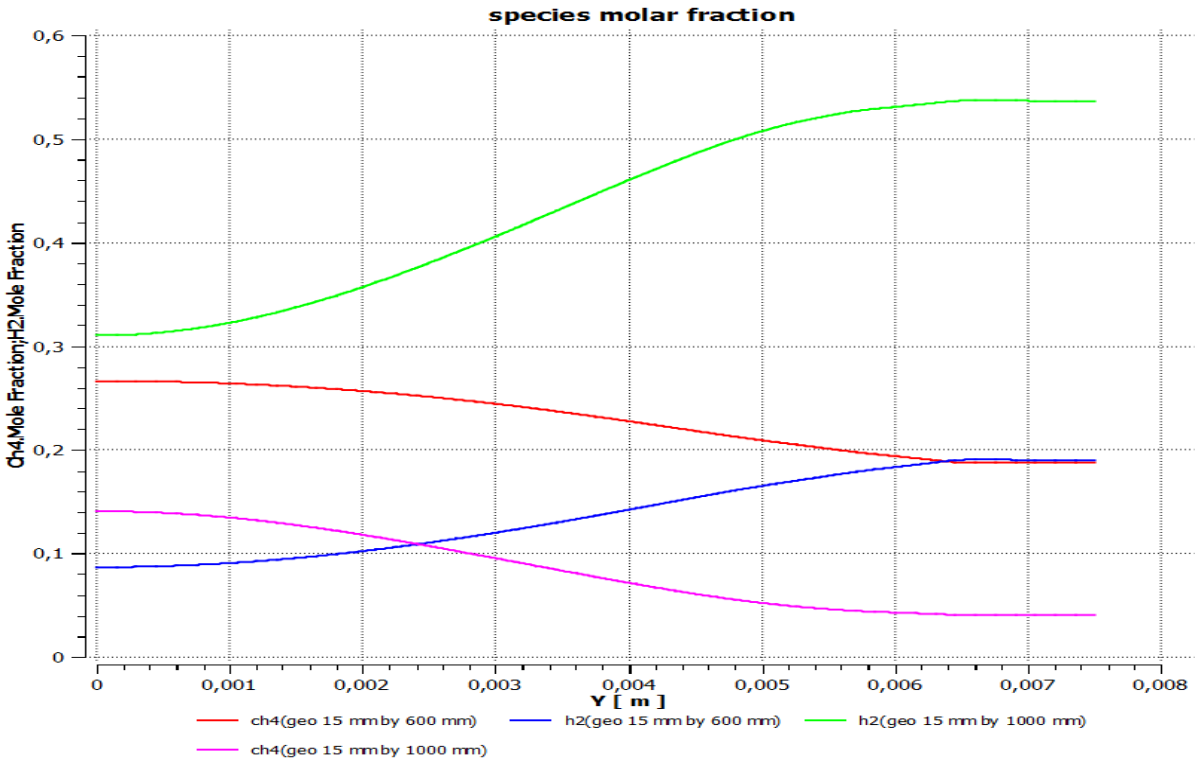

Figure 5.34: Radial profile of the methane and hydrogen molar fraction at the outlet of the tube for a tube length of 600 mm and 1000 mm.

As can be seen in figure 5.34, when the tube length is increased, the methane molar fraction at the outlet of the tube decreases. This means that more methane converted into hydrogen and this can be seen also in figure 5.34. The hydrogen molar fraction increased at the outlet of the tube. The methane conversion increased from 22.69% to 72.43% and hydrogen yield increased from 23.48% to 73.99%. The temperature and velocity contour plot of the geometry with length of $1000mm$ is given below. The boundary condition are as follows : The particle mass fraction is 10^{-4}, the methane inlet molar fraction is 0.297 and the wall heat flux is set at $10KW$.

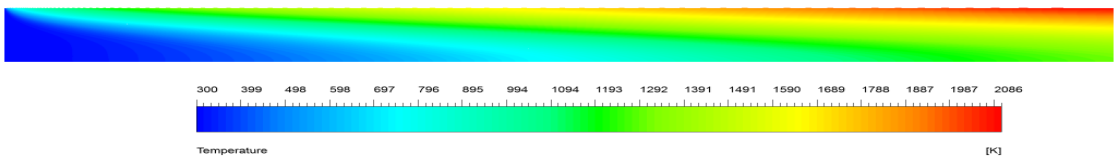

Figure 5.35: The temperature plot for a case with longer reactor tube.[other parameters identical to those of case 1]

The temperature plot of case 3 is given in figure 5.35. As can be seen the maximum temperature is $2066K$ which is higher than $1766K$ for case 1. But in practice we can not use such high temperature although increasing the temperature leads to higher methane conversion.

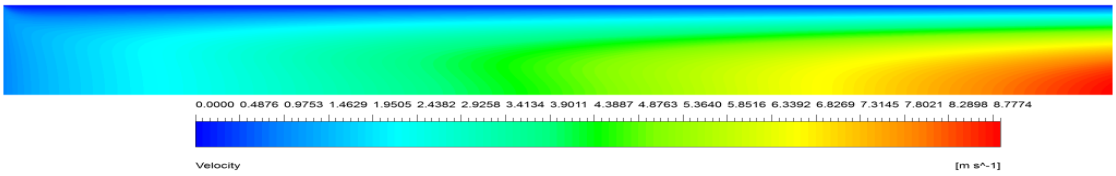

Figure 5.36: Velocity plot for a case with longer reactor tube.[other parameters identical to those of case 1]

.

The fluid velocity plot is shown in figure 5.36. The maximum velocity is $8.78\frac{m}{s}$ which is higher than $7.75\frac{m}{s}$ found in case 1. This is because of the higher temperature found in the system. Due to this the fluid expands more than in case 1 and due to this the velocity increases.

5.5. Influence of the wall heat flux

The influence of the wall heat flux is examined to see how the methane and hydrogen conversion is improved. In this case the wall heat flux is increased from $10kW$ to $15kW$. The reference simulation is case 1 and all other parameters are kept constant as shown in table 5.3. In this section the methane and hydrogen molar fraction at the outlet of the tube in the radius direction is shown in figure 5.37.

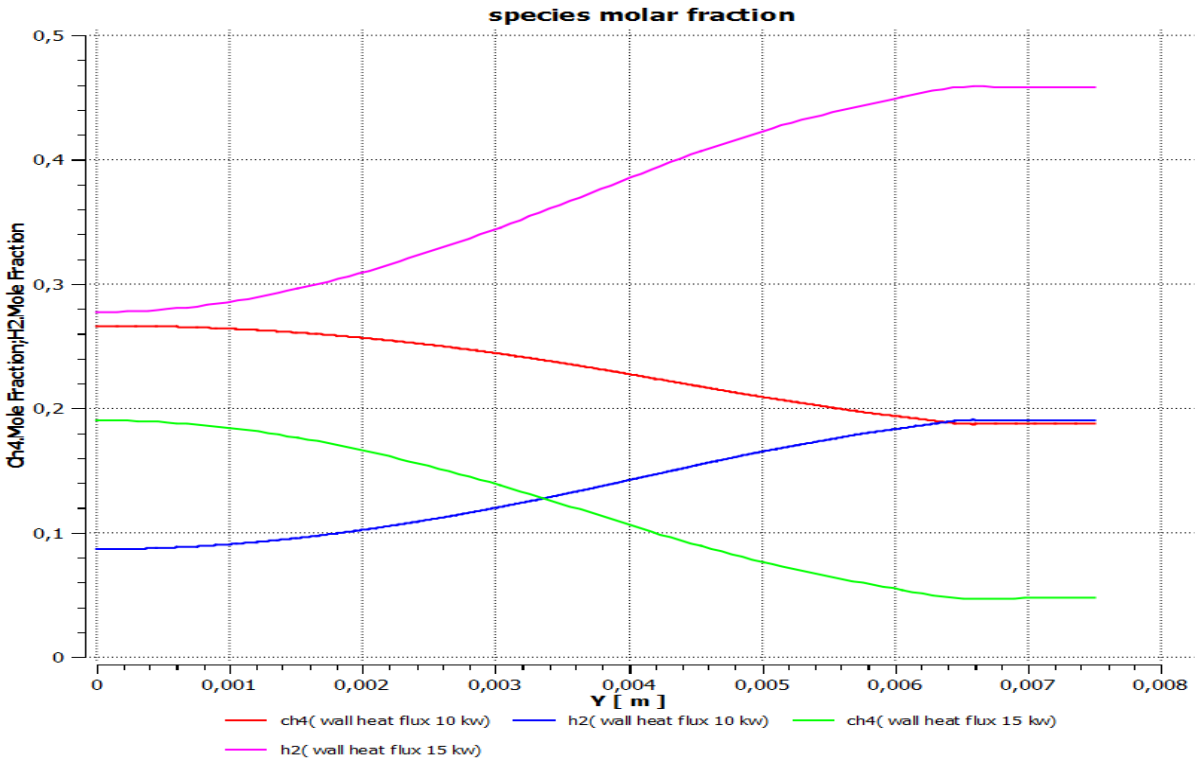

Figure 5.37: Methane and hydrogen molar fraction at the outlet of the tube in the radius direction for wall heat flux of 10 kw and 15 kw.

In figure 5.37 the influence of increasing wall heat flux on the molar fraction at the outlet is shown. The methane molar fraction at the outlet decreases when the wall heat flux is increased and the hydrogen molar fraction increased. The result is that methane conversion increased from 22.69% to 61.31% and hydrogen yield increased from 23.28% to 62.99%.

The temperature and velocity plot is shown for a wall heat flux of $15kW$. The boundary condition for this case (case 4) is as follow: the particle volume fraction is 10^{-4}, the methane inlet molar volume is 0.297 and the reactor length is $600mm$.

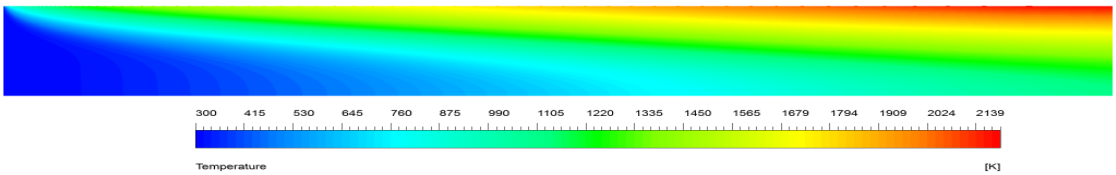

Figure 5.38: The temperature plot for a case with higher wall heat flux.[other parameters identical to those of case 1]

The maximum temperature in case 4 is shown in figure 5.38 which is $2135K$. The maximum temperature of case 1 which is 1766 is significantly lower the maximum temperature found in figure 5.38. As discuss before the temperature is to high found in case 4 which is not acceptable in practice. But due to the high temperature the methane conversion increase as will discuss below.

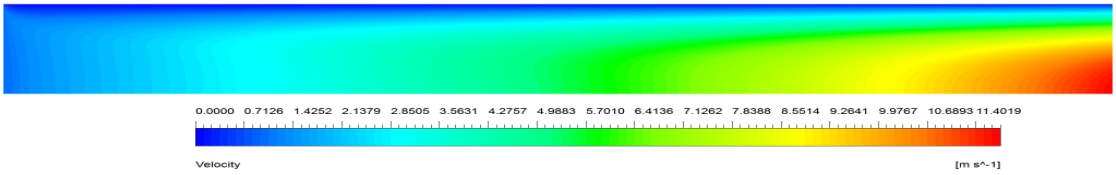

Figure 5.39: Velocity plot for a case with higher wall heat flux.[other parameters identical to those of case 1]

The same can be sad for the velocity in case 4. The maximum velocity is $11.40\frac{m}{s}$ in figure 5.39. This maximum velocity is higher than $7.75\frac{m}{s}$ in case 1. This could be again due to high temperature in the system.

5.6. Influence of methane inlet molar fraction

The influence of the methane inlet molar fraction on the methane and hydrogen conversion was examined. At the inlet of the tube the methane molar fraction was decreased from 0.297 to 0.1. The reference case is case 1 as shown in table 5.3 and all other parameters are kept constant. The methane and hydrogen molar fraction at the out of the tube in the radius direction is plotted in figure 5.40.

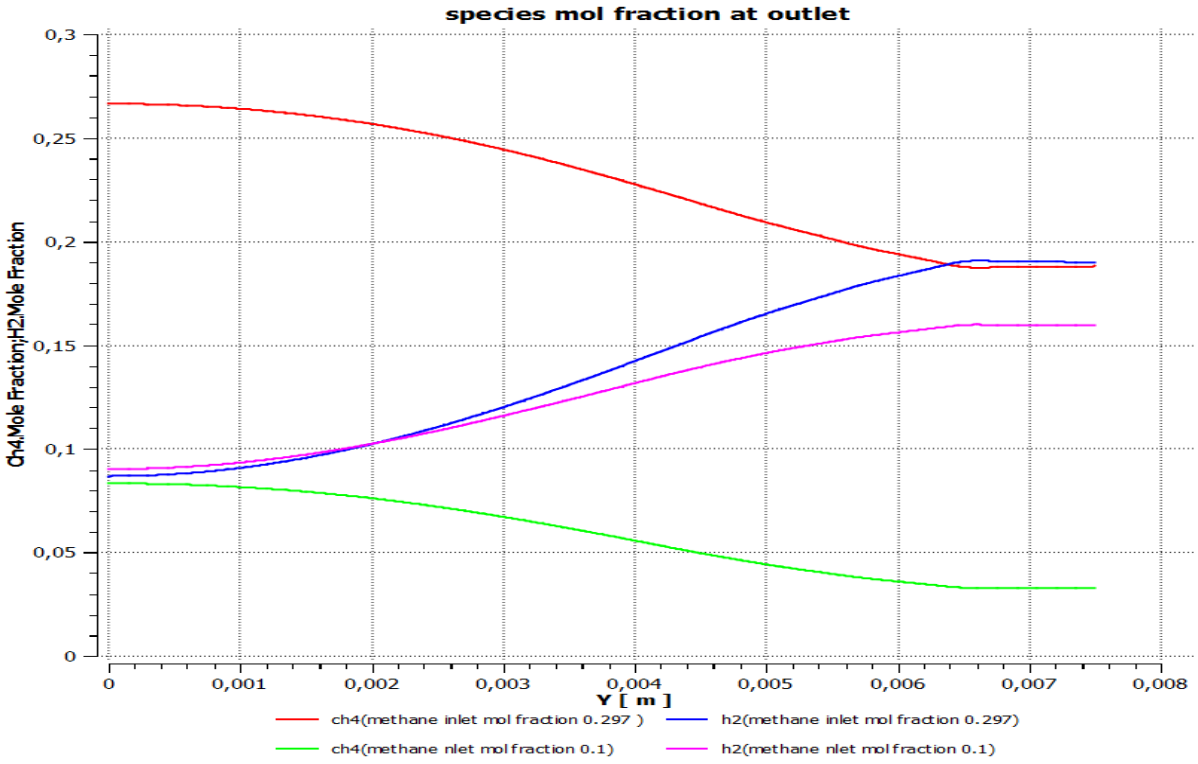

Figure 5.40: Methane and hydrogen molar fraction at the outlet of the tube in the radius direction for methane molar inlet fraction of 0.1 and 0.297.

As can be seen that in figure 5.40 the hydrogen molar fraction is higher at the outlet of the tube for methane inlet molar fraction of 0.297. The methane conversion is increased from 22.69% to 42.19% and hydrogen yields increased from 23.28% to 63.86%. From this can be concluded that when the methane inlet molar fraction is lower at the inlet, the conversion of methane is higher and the hydrogen yield is also higher.
The temperature and velocity plot is shown below for methane inlet molar fraction of 0.1. The boundary condition are as follow: The particle volume fraction is 10^{-4}, the wall heat flux is $10KW$ and the reactor length is $600mm$.

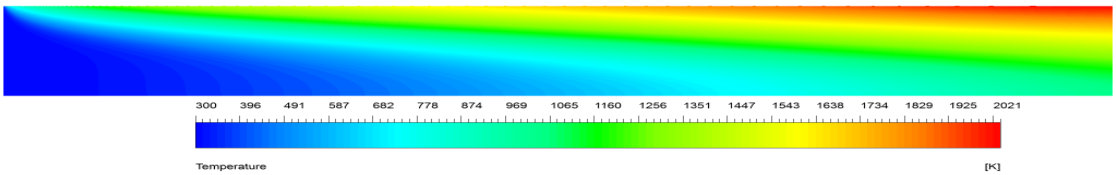

Figure 5.41: The temperature plot for a case with lower methane inlet molar fraction.[other parameters identical to those of case 1]

The temperature plot of case 5 is shown in figure 5.41. When the methane inlet molar fraction is reduce to 0.1 the maximum temperature found in case 5 is $2021K$. This temperature is higher than in case 1 which is $1766K$.

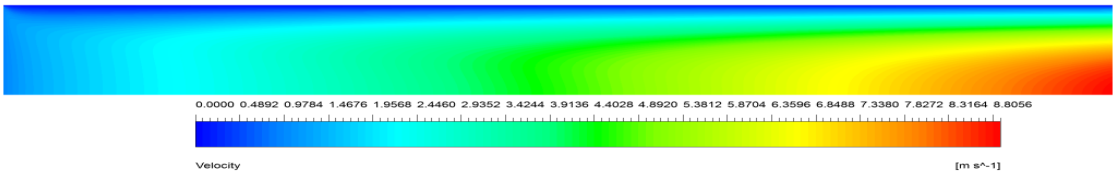

Figure 5.42: Velocity plot a case with lower methane inlet molar fraction.[other parameters identical to those of case 1]

The maximum velocity for case 5 is $8.81\frac{m}{s}$ which is higher than $7.75\frac{m}{s}$ found in case 1. The could be due to higher temperature in the system.

5.7. Summary of the simulation cases

In this section The methane conversion and hydrogen yield of each cases is given in a table.

Case number	Methane conversion (%)	hydrogen yield (%)
Case 1	22	23
Case 2	12	12
Case 3	72	74
Case 4	61	63
Case 5	42	64

Table 5.4: Methane conversion and hydrogen yields

Below all the simulated cases are listed in the table 5.5 with the initial condition.

Case number	Initial particle diameter size $[\mu m]$	Initial particle velocity $[\frac{m}{s}]$	Particle inlet volume fraction [–]	Methane inlet molar fraction [–]	wall heat flux [kW]	length of tube [mm]
Case 1	30	10^{-3}	10^{-4}	0.297	10	600
Case 2	30	10^{-3}	10^{-5}	0.297	10	600
Case 3	30	10^{-3}	10^{-4}	0.297	10	1000
Case 4	30	10^{-3}	10^{-4}	0.297	15	600
Case 5	30	10^{-3}	10^{-4}	0.1	10	600

Table 5.5: Initial conditions for all simulated cases

6

Conclusion and Recommendation

6.1. Conclusion

In the present work an overview of the solar reactor design development throughout the years is given. The solar reactors found in the literature study have been divided into five groups. Because from the summary in table 5.1 there was no clear indication which solar reactor was the best to build on industrial scale, a simplified numerical simulation was performed on a tube reactor in order to gain more understanding. The reactor of Caliot in Caliot *et al.* [7] is taken as reference reactor because of it simple geometry. In table 5.1 a summary given of model used in Caliot work and the model used in this work. As can be seen from table 5.1 the particle process are simplified in this work and only heterogeneous reaction is taken account. Also the radiation properties is simplified. To validate the present work we can qualitatively compare the result with the work done by Caliot. The influence of the particle mass fraction, wall heat flux, geometry length and methane inlet molar fraction was examined. It is found that increasing the particle mass fraction, wall heat flux and the geometry length increased the methane conversion and hydrogen yield. When the methane inlet molar fraction is decreased from 0.297 to 0.1 there was significantly increased in methane conversion and hydrogen yield. At this stage it is hard to say which reactor type is better comparing with the data in table 2.1. But based on the simplicity and on the methane conversion the cavity receiver tube reactor must be further improved. As shown in table 2.1 the methane conversion can be higher than what is reach in present work.

6.2. Recommendation

In this work a numerical study is made and it is investigate how to improve the methane conversion and hydrogen production in a solar reactor. In order to predict more directly the methane conversion in the solar reactor investigate in this work improvements and extensions are recommended:

First the model improvements:

- Improve chemistry: The reaction rate is base on a single step methane cracking propose by Maag . To account for the production of byproduct more detailed reaction rate is needed.
- Radiation model: For the methane absorption coefficient instead of Planck mean absorption coefficient another absorption model must be used.
- Absorption coefficient: influence of absorption coefficient if Radiation heat transfer is dominant.

Second Extension for other reactor types

- Turbulent flow: In the present the flow is laminar. When the reactor will scale up the flow will become turbulent. Due to this the particle flow will be different an also the heat will mix more effectively.

Last Other issue

- The particle deposition model must be included.

Bibliography

[1] S. Rodat, S. Abanades, J.-L. Sans, and G. Flamant, *Hydrogen production from solar thermal dissociation of natural gas: development of a 10kw solar chemical reactor prototype,* Solar Energy **83**, 1599 (2009).

[2] S. Abanades, H. Kimura, and H. Otsuka, *A drop-tube particle-entrained flow solar reactor applied to thermal methane splitting for hydrogen production,* Fuel **153**, 56 (2015).

[3] D. Hirsch and A. Steinfeld, *Radiative transfer in a solar chemical reactor for the co-production of hydrogen and carbon by thermal decomposition of methane,* Chemical Engineering Science **59**, 5771 (2004).

[4] S. Abanades and G. Flamant, *Solar hydrogen production from the thermal splitting of methane in a high temperature solar chemical reactor,* Solar Energy **80**, 1321 (2006).

[5] N. Ozalp, M.-H. Chien, and G. Morrison, *Computational fluid dynamics and particle image velocimetry characterization of a solar cyclone reactor,* Journal of Solar Energy Engineering **135**, 031003 (2013).

[6] M. F. Modest, *Radiative heat transfer* (Academic press, 2013).

[7] C. Caliot, G. Flamant, G. Patrianakos, M. Kostoglou, and A. G. Konstandopoulos, *Two-dimensional model of methane thermal decomposition reactors with radiative heat transfer and carbon particle growth,* Aiche Journal **58**, 2545 (2012).

[8] D. Cao, Y. Sun, and G. Wang, *Direct carbon fuel cell: fundamentals and recent developments,* Journal of Power Sources **167**, 250 (2007).

[9] A. Rubino, *Theorical modeling of laminar and turbulent dispersed multiphased flow in a solar reactor for hydrogen production by cracking of methane,* .

[10] S. Rodat, S. Abanades, J. Coulié, and G. Flamant, *Kinetic modelling of methane decomposition in a tubular solar reactor,* Chemical Engineering Journal **146**, 120 (2009).

[11] S. Rodat, S. Abanades, J.-L. Sans, and G. Flamant, *A pilot-scale solar reactor for the production of hydrogen and carbon black from methane splitting,* International Journal of Hydrogen Energy **35**, 7748 (2010).

[12] G. Maag, S. Rodat, G. Flamant, and A. Steinfeld, *Heat transfer model and scale-up of an entrained-flow solar reactor for the thermal decomposition of methane,* international journal of hydrogen energy **35**, 13232 (2010).

[13] M. Gautier, V. Rohani, L. Fulcheri, and J. P. Trelles, *Influence of temperature and pressure on carbon black size distribution during allothermal cracking of methane,* Aerosol Science and Technology **50**, 26 (2016).

[14] D. Trommer, D. Hirsch, and A. Steinfeld, *Kinetic investigation of the thermal decomposition of ch 4 by direct irradiation of a vortex-flow laden with carbon particles,* International Journal of Hydrogen Energy **29**, 627 (2004).

[15] N. Ozalp and D. JayaKrishna, *Cfd analysis on the influence of helical carving in a vortex flow solar reactor,* international journal of hydrogen energy **35**, 6248 (2010).

[16] D. Hirsch and A. Steinfeld, *Solar hydrogen production by thermal decomposition of natural gas using a vortex-flow reactor,* International Journal of Hydrogen Energy **29**, 47 (2004).

[17] M. Kogan and A. Kogan, *Production of hydrogen and carbon by solar thermal methane splitting. i. the unseeded reactor,* International Journal of Hydrogen Energy **28**, 1187 (2003).

[18] S. Abanades and G. Flamant, *Experimental study and modeling of a high-temperature solar chemical reactor for hydrogen production from methane cracking,* International journal of hydrogen energy **32**, 1508 (2007).

[19] D. J. Krishna and N. Ozalp, *Numerical investigation of particle deposition inside aero-shielded solar cyclone reactor: A promising solution for reactor clogging,* International Journal of Heat and Fluid Flow **40**, 198 (2013).

[20] V. Shilapuram, D. J. Krishna, and N. Ozalp, *Residence time distribution and flow field study of aero-shielded solar cyclone reactor for emission-free generation of hydrogen,* international journal of hydrogen energy **36**, 13488 (2011).

[21] J. K. Dahl, K. J. Buechler, A. W. Weimer, A. Lewandowski, and C. Bingham, *Solar-thermal dissociation of methane in a fluid-wall aerosol flow reactor,* International Journal of Hydrogen Energy **29**, 725 (2004).

[22] J. Wyss, J. Martinek, M. Kerins, J. K. Dahl, A. Weimer, A. Lewandowski, and C. Bingham, *Rapid solar-thermal decarbonization of methane in a fluid-wall aerosol flow reactor–fundamentals and application,* International journal of chemical reactor engineering **5** (2007).

[23] F. U. Manual, *Fluent inc,* Chapter **6**, 14 (2003).

[24] A. Fluent, *12.0 udf manual,* Ansys Inc (2009).

A

Nomenclature

ρ	Density
t	Time
u	Velocity
P	Pressure
τ_{ij}	Viscous stress tensor
μ	Dynamic viscosity
λ_c	Thermal conductivity
δ_{ij}	Delta
y_k	Species mass fraction
$J_{k,j}$	Mass flux
R_k	Reaction rate
$D_{k,g}, D_{AB}$	mixture diffusion constant pf species
H	Enthalpy
T	Temperature
S_{rad}	Radiation heat source
c_p	heat capacity
x	space cordinate
q_{rad}	Radiation flux
σ	Stefan Boltzman constant
Re	Reynolds number
Sc	Schmidt number
Da	Damhohler number
Pr	Prandtl number
Pl	Planck number
T_{ref}	Reference temperature
$e_{\lambda,b}$	Black body power
λ	Wavelength
c_o	Speed of light
n	Refractive index
$I_{b\lambda}$	Black body spectral intensity
I_λ	Spectral intensity
$I_{\lambda,abs}$	Spectral intensity contribute by absorption
$I_{\lambda,emit}$	Spectral intensity contribute by emitting
$I_{\lambda,scat}$	Spectral intensity contribute by scattering
κ_λ	Absorption coefficient
$\sigma_{s\lambda}$	Scattering coefficient
$\phi_{\lambda s}$	Scattering phase function
$\hat{s}$	Beam traveling path
d_p	Particle diameter

ξ	Particle size parameter
k_B	Boltzman constant
f_v, α_p	Particle volume fraction
Q_{abs}	Absorption coefficient
Q_{scat}	Scattering coefficient
N_p	Number of particle per volume
C_{abs}	Absorption cross section
C_{scat}	Scattering cross section
an, bn	Expansion coefficient(Mie Theory)
ψ_n, α_n	Ricatte-Bessel function
m	Refractive index ratio
τ_λ	Optical thickness
ρ_s	Carbon density
τ	Reaction time scale
V_p	Particle volume
V	Total volume
m_s	Particle mass
r_{ch4}	Methane reaction rate
r_{h2}	Hydrogen reaction rate
r_c	Carbon reaction rate
θ	Field variable
m_{ch4}	Methane molar mass
m_{h2}	Hydrogen molar mass
m_c	Carbon molar mass
a_p	Equivalent absorption coefficient
σ_p	Equivalent scattering coefficient
$m_{p,in}$	Particle mass flow rate
ν	Kinematic viscosity
D	Reactor Diameter
X_{ch4}	Methane conversion
X_{h2}	Hydrogen conversion
h	Planck constant
$I_{\lambda,isc}$	Spectral intensity contribute by incoming scattering
π	pi
R	Universal gas constant
F_{Ch4}	Methane molar fraction
F_{h2}	Hydrogen molar fraction
$V_{g,in}$	Flow rate
ρ_p	Particel density